


2021-05-01

A Study Of The Frustrated Honeycomb Battery Material Na₂Ni₂TeO₆

Nathan Christopher Episcopo
University of Texas at El Paso

Follow this and additional works at: https://scholarworks.utep.edu/open_etd

 Part of the [Condensed Matter Physics Commons](#), [Mechanics of Materials Commons](#), and the [Oil, Gas, and Energy Commons](#)

Recommended Citation

Episcopo, Nathan Christopher, "A Study Of The Frustrated Honeycomb Battery Material Na₂Ni₂TeO₆" (2021). *Open Access Theses & Dissertations*. 3246.
https://scholarworks.utep.edu/open_etd/3246

This is brought to you for free and open access by ScholarWorks@UTEP. It has been accepted for inclusion in Open Access Theses & Dissertations by an authorized administrator of ScholarWorks@UTEP. For more information, please contact lweber@utep.edu.

A STUDY OF THE FRUSTRATED HONEYCOMB BATTERY MATERIAL

NA₂NI₂TEO₆

NATHAN CHRISTOPHER EPISCOPO

Master's Program in Physics

APPROVED:

Harikrishnan Nair, Ph.D., Chair

Rajendra Zope, Ph.D.

Thomas W. Heitmann, Ph.D.

Stephen L. Crites, Jr., Ph.D.
Dean of the Graduate School

Copyright ©

by

Nathan Episcopo

2021

A STUDY OF THE FRUSTRATED HONEYCOMB BATTERY MATERIAL

$\text{Na}_2\text{Ni}_2\text{TeO}_6$

by

NATHAN CHRISTOPHER EPISCOPO

BSc

THESIS

Presented to the Faculty of the Graduate School of

The University of Texas at El Paso

in Partial Fulfillment

of the Requirements

for the Degree of

MASTER OF SCIENCE

Department of Physics

THE UNIVERSITY OF TEXAS AT EL PASO

May 2021

Abstract

The P2-type layered hexagonal compound $\text{Na}_2\text{Ni}_2\text{TeO}_6$ with Ni^{2+} on a honeycomb lattice was synthesized by the standard solid-state route. Structural characterization chemical phase purity was confirmed by Rietveld refinement of laboratory and synchrotron data. The crystal structure refines well in the $P6_3/mcm$ space group. Single crystal growth trials using the self-flux-melt method were conducted with limited success. The magnetic transition temperature pertaining to Ni^{2+} lattice was confirmed by analysis of specific heat capacity to be $T_N = 27 \text{ K}$. The magnetic susceptibility remains largely unchanged in magnetic field of $H = 80 \text{ kOe}$ and external pressure of $P = 1.2 \text{ GPa}$. There is an almost linear response in isothermal magnetization up to $H = 130 \text{ kOe}$. The nuclear structure studied using high resolution neutron diffraction data confirms the results from refinement of synchrotron data. Four different magnetic structure models were used to quantitatively analyze $T = 5 \text{ K}$ neutron diffraction data, with the best fitting model consisting of two commiserate propagation vectors $\vec{k}_c = (0.5 \ 0 \ 0)$ and $\vec{k}_c = (0.5 \ 0 \ 0.5)$ with an additional profile term to account for short-range ordering. The long-range magnetic structure produced by the multi-phase model consist of 2D in-plane (ab) zig-zag ferromagnetic chains and are antiferromagnetically arranged in adjacent chains. Inelastic neutron scattering shows $\text{Na}_2\text{Ni}_2\text{TeO}_6$ has a spin wave excitation with energy $E \approx 5 \text{ meV}$ at $T = 5 \text{ K}$.

Table of Contents

Abstract	iv
Table of Contents	v
List of Tables	vii
List of Figures	vii
Chapter 1: Introduction	14
1.1 P2 Type Layered Honeycomb Struture.....	1
1.1.1 Strong Ion condutor (Possible Cathode Material in Sodium Ion Batteries)	1
1.2 Magnetic Properties	2
1.2.1 Magnetic Structure	2
1.2.2 Magnons and Spin Gab Behavior	3
1.2.3 Kitaev Model and J_1 - J_2 - J_3 Model.....	4
Chapter 2: Crystallography,.....	7
2.1 Crystal Structutre	7
2.1.2 Unit Cell and Bravais Lattice	7
2.1.3 Reciprocal Lattice	8
2.2 Symmetry and Space Group.....	10
2.3 Lattice Planes	11
2.4 The Crystal Structure of $\text{Na}_2\text{Ni}_2\text{TeO}_6$	12
Chapter 3: Synthesis and Crystal Growth.....	14
3.1 Shake ‘n Bake Method.....	14
3.1.1 Sythesizing $\text{Na}_2\text{Ni}_2\text{TeO}_6$	17
3.2 Self Flux-Melt Method of Crystal Growth	18
Chapter 4: X-Ray and Neutron Diffraction ,	21
4.1 Basics of Diffraction Theory and Powered Diffraction	21
4.2 Powder X-Ray Diffraction	24
4.2.1 Scattered X-ray Amplitudes	26
4.2.2 Powder X-Ray Diffractometers	27
4.3 Powder Neutron Diffraction	30

4.4 Rietveld Refinement	32
4.4.1 Rietveld Refinement of Powder X-Ray and Neutron Diffraction data For Na ₂ Ni ₂ TeO ₆	33
4.5 Solving the Magnetic Structure Using SARAh	37
4.5.1 The Magnetic Structure of Na ₂ Ni ₂ TeO ₆	39
4.6 Inelastic Neutron Diffraction	42
4.6.1 Inelastic Neutron Scattering of Na ₂ Ni ₂ TeO ₆	43
Chapter 5: Bulk Properties of Na ₂ Ni ₂ TeO ₆ ,.....	46
5.1 Heat Capacity and Entropy	46
5.1.2 Specific Heat Capacity of Na ₂ Ni ₂ TeO ₆	47
5.2 Measuring Magnetic Susceptibility	49
5.2.1 Curie-Weiss Law and Fitting	50
5.2.2 Magnetic Susceptibility of Na ₂ Ni ₂ TeO ₆	53
Chapter 6: Summary and future work,.....	55
6.1 Summary	55
6.2 Future Work	56
References.....	57
Vita.....	60

List of Tables

Table 1.1: Measured Ion Conductivities (S m^{-1}) for two $\text{Na}_2\text{M}_2\text{TeO}_6$ compounds.....	2
Table 2.1: The 14 Bravais lattice systems.....	9
Table 2.2: Crystal Systems and Symmetry.....	10
Table 4.1: Refined atomic positions of $\text{Na}_2\text{Ni}_2\text{TeO}_6$ at 295 K and 5K refined from neutron data obtained from BT-1 instrument.....	37
Table 4.2: A table of the four magnetic structure models used for the analysis of neutron diffraction pattern at $T = 5 \text{ K}$. The fitting residuals are tabulated, R_p , R_{wp} , R_B , R_{mag} , to provide quantitative comparison of the four models.....	42

List of Figures

Figure 1.1: Magnetic substitutability curves for polycrystalline (black line) and single crystal (green line along ab plane, blue line along c-axis) $\text{Na}_2\text{Ni}_2\text{TeO}_6$	2
Figure 1.2: (A.) Diagram of the Kitaev honeycomb lattice made up of three different bonds (B.) The three bonds in the Kitaev model.....	5
Figure 1.3: Diagram showing the three spin exchange interactions J_1 - J_2 - J_3 with solid and empty circles forming two sublattices and t_2 , t_1 are the unit cell translation vectors for a honeycomb lattice.....	6
Figure 2.2: Lattice planes with Miller indices.....	11
Figure 2.3: (A.) The a-b plane of $\text{Na}_2\text{Ni}_2\text{TeO}_6$ showing the hexagonal pattern of nickel cations (green spheres), and $a_1 = a_2$ lattice constants of the unit cell. (B.) The c-b plane of $\text{Na}_2\text{Ni}_2\text{TeO}_6$ with the c_1 lattice constant of the unit cell.....	13
Figure 3.1: (1.) Initially cations (B^+ , A^+) are diffused through the reagents and adsorbed at crystal defect sites on the surfaces of the reagents.(2.). After some time the product layer (A_pB_q) grows with the cations diffusing through the product towards the surfaces of the reagents. The size of the product layer is limited by the diffusion pathlength.....	15
Figure 3.2: (1.) Similar crystal structure between reagents and product results in stable product growth as dendrites. (2.) Dissimilar crystal structure of product and reagents results in unstable product growth with product layers that break away from the reagents surfaces.....	16
Figure 3.3: (1.) A. Precursor Powder. B. Pure Chemical Phase $\text{Na}_2\text{Ni}_2\text{TeO}_6$ (2.) A SEM micrograph of a sintered pellet of $\text{Na}_2\text{Ni}_2\text{TeO}_6$, grain size $\sim 5 - 20 \mu\text{m}$	18
Figure 3.4: (1.) The incomplete $\text{Na}_2\text{Ni}_2\text{TeO}_6$ and flux mixture of the first trial. (2.) Small $\text{Na}_2\text{Ni}_2\text{TeO}_6$ crystals from the second trial.....	20
Figure Figure 4.1: Schematic diagram of diffracted waves interfering.....	21
Figure 4.2: (A.) Diagram of coherent waves being diffracted by diffraction grating with slit spacing d of by an angel $d \sin\theta$. (B.) The ordered arrangement of atoms in a crystal form planes that are a set distance (d -spacing) apart from adjacent parallel planes – producing a diffraction grating.....	22

Figure 4.3: An illustration of the parameters for constructive interference of waves diffracted by adjacent atomic planes - Bragg's law. When the difference in path length ($2d \sin\theta$) is equal to an integer of the wavelength ($n\lambda$) the waves will constructively interfere.....23

Figure 4.4: The transition of higher orbital electrons to fill the vacant orbital of an ionized Cu atom.....28

Figure 4.5: Diagram of the typical X-ray tube used in a PXRD diffractometer.....28

Figure 4.6: A diagram of the Bragg-Brentano configuration of PXRD with the bisecting diffraction vector \mathbf{S} kept normal to the sample surface.....29

Figure 4.7: Diagram of the 11-BM Diffractometer at APS Argonne.....30

F Figure 4.7: Graphs of Rietveld refinement (FullProf) of powder diffraction data for $\text{Na}_2\text{Ni}_2\text{TeO}_6$ measured on three different diffractometers.

A. Laboratory PXRD (Inset shows zoom-in lower portion of first peak)

B. Synchrotron light source PXRD ($T = 100\text{ K}$)

C. High resolution neutron powered diffraction ($T = 295\text{ K}$).....35

Figure 4.8: The neutron diffraction patterns above the magnetic transition temperature (black circles) and below the transition (green dots), the inset shows a zoomed in portion of plots where two magnetic peaks in the 5 K data are present.....39

F Figure 4.9: Ni cations on a honeycomb lattice (green spheres) with the magnetic moments (red arrows) arranged in zig-zag ferromagnetic chains that are antiferromagnetically aligned with each other. The magnetic structure is determined from the neutron diffraction data on $\text{Na}_2\text{Ni}_2\text{TeO}_6$ at 5 K obtained from BT-1 instrument.....41

Figure 4.10: (a) The Rietveld refinement plot of $\text{Na}_2\text{Ni}_2\text{TeO}_6$ neutron diffraction data at $T = 5\text{ K}$ obtained from BT-1, incorporating nuclear structure in the $P63/mcm$ space and two-phase magnetic model with a commensurate $\vec{k}_c(0.5\ 0\ 0)$ and incommensurate $\vec{k}_{ic}(0.47\ 0.44\ 0.28)$ propagation vectors.

(b) The Rietveld refinement plot of $\text{Na}_2\text{Ni}_2\text{TeO}_6$ neutron diffraction data at $T = 5\text{ K}$, incorporating nuclear structure in the $P63/mcm$ space and two-phase magnetic model with commensurate propagation vectors $\vec{k}_c(0.5\ 0\ 0)$ and $\vec{k}_c(0.5\ 0\ 0.5)$ and short-range order.....42

Figure 4.11: A schematic of a triple axis neutron spectrometer.....43

Figure 4.12: (a) Intensity of inelastic scattered neutrons at $T = 35\text{ K}$ for three Q - values: 0.75 \AA^{-1} , 0.89 \AA^{-1} , and 1.0 \AA^{-1}

- (b) Intensity of inelastic scattered neutrons at $T = 5\text{ K}$ for three Q - values: 0.75 \AA^{-1} , 0.89 \AA^{-1} , 1.0 \AA^{-1} , and 2.09 \AA^{-1} , dashed lines are standard profile fits.
- (c) Constant- Q (0.75) E -scan at 5 K , 20 K , and 35 K .
- (d) Q - dependence of intensity at 5 K for $E = 2\text{ meV}$, $E = 5\text{ meV}$ and $E = 8\text{ meV}$ 45

Figure 5.0: A. The C_p/T of $\text{Na}_2\text{Ni}_2\text{TeO}_6$ the inset shows a second order transition at $T = 27\text{ K}$.
 B. C_p/T of $\text{Na}_2\text{Zn}_2\text{TeO}_6$ a phonon analog of $\text{Na}_2\text{Ni}_2\text{TeO}_6$.
 C. C_p/T of $\text{Na}_2\text{Ni}_2\text{TeO}_6$ (x-scale \log_{10}) shows a broad feature at $\sim 100\text{ K}$ indicating short-range magnetic order transition.
 D. The C_p/T versus T of the specific heat capacity of $\text{Na}_2\text{Ni}_2\text{TeO}_6$ with specific heat capacity of $\text{Na}_2\text{Zn}_2\text{TeO}_6$ subtracted (the phonon contribution) supporting the magnetic nature of the transition at $T = 27\text{ K}$.
 E. The magnetic entropy (S_m/T) of $\text{Na}_2\text{Ni}_2\text{TeO}_6$ with the largest change occurring around $T \approx 27\text{ K}$4
 9

F Figure 5.2: A. Magnetic susceptibility of $\text{Na}_2\text{Ni}_2\text{TeO}_6$ at 50 Oe with zero pressure and 1.2 GPa .
 B. Magnetic susceptibility of $\text{Na}_2\text{Ni}_2\text{TeO}_6$ at 0.5 T and 8 T .
 C. AC Magnetic susceptibility of $\text{Na}_2\text{Ni}_2\text{TeO}_6$ measured at 0.1 Hz , 1 Hz , 10 Hz , 100 Hz , and 1000 Hz with an applied field of 50 Oe53

Chapter 1: Introduction

1.1 P2 Type layered honeycomb structure

The metal oxide $\text{Na}_2\text{Ni}_2\text{TeO}_6$ exhibits several interesting properties including long- and short-range magnetic ordering, high ionic conductivity, and disordered Na ion interlayer with a possible chiral structure (1,2,3). This compound has a hexagonal closed-packed crystal structure where Ni octahedra forming a honeycomb lattice with Te octahedra located in the center of the nickel honeycombs. It is an example of a P2-type layered compound where the interlayer of Van der Waals bound Na^+ ions from triangular prisms with O in the layers made up of Ni and Te octahedra. $\text{Na}_2\text{Ni}_2\text{TeO}_6$ stands out from other similarly structured compounds by having columns consisting of only Te or Ni atoms when viewed along the c -axis. This is opposed to columns along the c -axis made up of alternating Te and M atoms for all other $\text{Na}_2\text{M}_2\text{TeO}_6$ compounds ($M = \text{Cu}, \text{Co}, \text{Zn}, \text{Mg}$) (1). This structure produces a complex potential field that has been proposed to cause the weakly bound Na ion interlayer to conduct in a chiral pattern (3).

1.1.2 Strong Ion conductor - possible cathode material in sodium ion batteries

There is particular interest in P2-type layered compounds due to their electrochemical properties that endow them the potential to serve as an electrode material in ion batteries. Their potential use in energy storage devices is in virtue of the observed high ionic conduction between layers of metal oxides in these. In $\text{Na}_2\text{M}_2\text{TeO}_6$ ($M = \text{Cu}, \text{Co}, \text{Ni}, \text{Mg}$) Na^+ cations are disorderly arranged, and weakly bound to the M -Te octahedra layers they are arranged between. These Na^+ cations offer low impedance to their transport in the presence of an external electric field. Materials that exhibit high migration of positive charge-carrying Na ions can have an application as a cathode material in sodium ion batteries. (1)

Table 1.1: Measured Ion Conductivities (S m^{-1}) for two $\text{Na}_2\text{M}_2\text{TeO}_6$ compounds (1).

Compound	Ion Conductivities (S m^{-1})	
	25°C	300°C
$\text{Na}_2\text{Ni}_2\text{TeO}_6$	0.0008 - 0.0034	10.1-10.8
$\text{Na}_2\text{Zn}_2\text{TeO}_6$	0.009	5.1- 7.0

1.2 Magnetic properties

Nickle is the magnetic species in $\text{Na}_2\text{Ni}_2\text{TeO}_6$ which leads to the magnetism of the compound. Nickel ($z = 28$) has two unpaired d -orbital spins with the electron configuration of $[\text{Ar}] 3p^8 4s^2$ giving a total spin $S = 1$ and an effective magnetic moment $2.83\mu_B$ per Ni atom. The oxidation state of Ni in $\text{Na}_2\text{Ni}_2\text{TeO}_6$ is +2 having its two most weakly bound electrons ($4s^2$) moving to full the valence band of the oxidizer. The magnetic substitutability curve for $\text{Na}_2\text{Ni}_2\text{TeO}_6$ shows a broad transition from the paramagnetic phase starting around $\sim 40 \text{ K}$ (4). Previous studies have identified an antiferromagnetic ordering at a T_N of $\sim 27\text{K}$ (4). Magnetic substitutability of a single crystal shows anisotropy with the crystallographic c -axis being the easy axis (4).

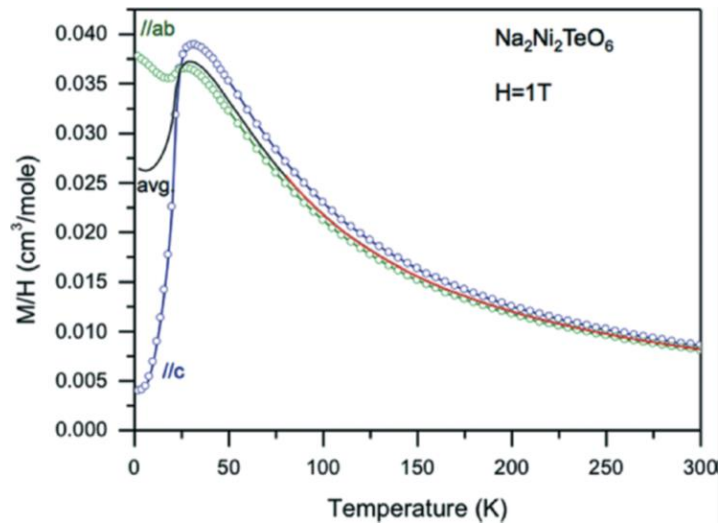


Figure 1.1: Magnetic substitutability curves for polycrystalline (black line) and single crystal (green line along ab plane, blue line along c -axis) $\text{Na}_2\text{Ni}_2\text{TeO}_6$ (4).

1.2.1 Magnetic structure

The magnetic structure of Ni^{2+} in $\text{Na}_2\text{Ni}_2\text{TeO}_6$ is of particular interest as it forms a honeycomb lattice in layers that are of significant distance ($\sim 11.14 \text{ \AA}$) from each other being separated by intercalated cations, setting up a quasi 2D arrangement. Such a magnetic structure has been theorized to have magnetic frustrations between spins that could produce novel quantum spin ground and excited states (6-7-9). Unlike other magnetically frustrated systems where frustration arises of mostly a geometrical arrangement of their spins (triangular and kagome lattices for example), any magnetic frustrations in a honeycomb lattice would; however, arise from a particular set of spin-spin interactions within the unit cell. These interactions are described by J_{ij} which are spin exchange interaction. The J_{ij} are coefficients of the spin overlap in the Heisenberg Hamiltonian,

$$\mathcal{H} = \sum_{ij} J_{ij} \mathbf{S}_i \cdot \mathbf{S}_j$$
 with \mathbf{S}_i being the spin operator (5). How a magnetic material orders is represented in the set J_n ; including the number of spin exchange (how many J_n), the strength of the interactions (magnitude of J_n), and how the spins align (sign of J_n). For $\text{Na}_2\text{Ni}_2\text{TeO}_6$ the spin interactions below the magnetic ordering critical temperature ($T_N \sim 27 \text{ K}$) has been shown to produce the following magnetic structure: 2D zig-zag chains of ferromagnetic aligned spins with each chain being antiferromagnetically aligned with each other adjacent spin chain in the Ni-Te plane (3).

Magnons 1.2.2

Materials that have ferromagnetic or antiferromagnetic ordering give rise to dynamic spin excitations called magnons. They are the magnetic moment analogue of the collective quantized crystal lattice vibrational modes in a solid, phonons. Both of these excitations (phonons and magnons) are the result of strong interactions between electrons in a many-body quantum

mechanical system, and they describe how energy is dispersed in their host materials. As such the collective behavior of quantum many-body systems can be mathematically treated as individual particle interacting with each other in free space; therefore, they are referred to as quasi-particles. Magnons are formed by the spin-spin coupling in magnetic materials where they exist as a quantized spin wave. They formed when an interacting spin system is perturbed, by scattered particle or thermal excitation, the with energy to sufficient to flip one spin:

$$\epsilon_k = \left(n_k + \frac{1}{2}\right) \hbar \omega \text{ where } \hbar \text{ is Plank's constant and } \omega \text{ is the angular frequency (5).}$$

A spin wave (magnon) is produced by energetically flipped spins due to the restrictions of spin states with only two allowed to have the same energy state if they have opposite spin states. When one spin is flipped, the spin; it is most strongly coupled with will respond to in accordance, which will in turn affect the spin coupled with the second spin and so on in a cascade fashion of flipping spins. This forms a propagating wave of flipping spins. $\text{Na}_2\text{Ni}_2\text{TeO}_6$ having a magnetic lattice consisting of 2D zig-zag spin chains that are antiferromagnetically ordered with adjacent chains is a spin configuration that could host unique and potentially useful magnons. The potential for spin chains to provided dispersion-less magnon transport along the quasi 2D layers of $\text{Na}_2\text{Ni}_2\text{TeO}_6$ could endow it with the properties needed for application in information processing (9). This would be as a material for magnonics - devices that utilize magnons the control of magnon transport in place of electron transport.

1.2.3 Kitaev model and J_1 - J_2 - J_3 model

A theoretical model by Alexei Kitaev is one of the currently prominent models to explain the magnetic frustrations on a honeycomb lattice with an exact solution (7). The Kitaev model is

a fashionable exactly solvable model for a 2D $s = \frac{1}{2}$ with Ising bond-centered nearest-neighbor interactions in a honeycomb lattice. The Kitaev Hamiltonian is: $\mathcal{H} = \sum_{(i,j)\gamma} K_{\gamma} S_i^{\gamma} \cdot S_j^{\gamma}$ with γ indexing the bond parallel to the easy axis, K is the exchange constant and S is spin operator (6). The Kitaev model predicts a quantum spin liquid ground state where symmetry breaking at the critical temperature is replaced by entropy reduction by long range spin entanglement resulting in absence of magnetic ordering down to very low temperatures (6).

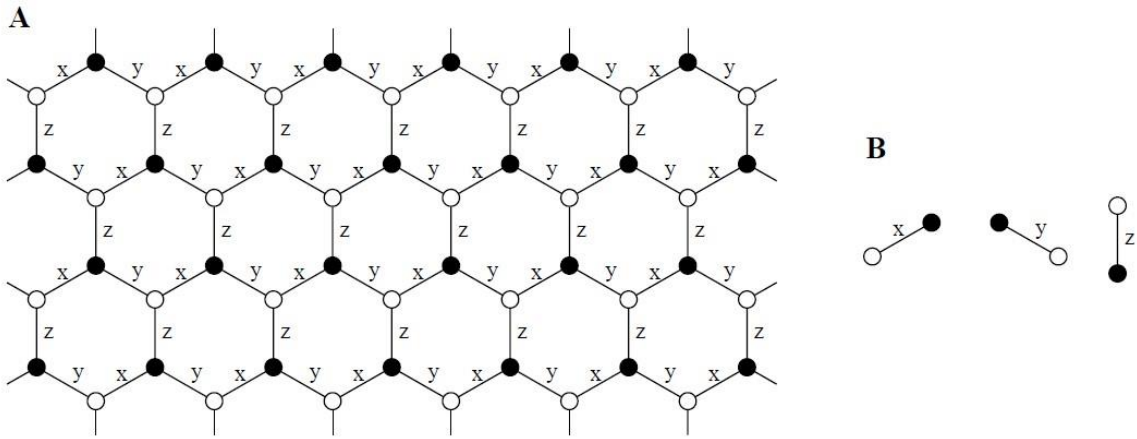


Figure 1.2: (A.) Diagram of the Kitaev honeycomb lattice made up of three different bonds (B.) The three bonds in the Kitaev model (7).

The $J_1 - J_2 - J_3$ model is the other popular model proposed to explain the correlated spin behavior of magnetic moments on a honeycomb lattice (8). This model is built upon three in-plane spin exchange interactions (J) for antiferromagnetically ordered honeycomb magnets. These interactions can be of ferromagnetic or antiferromagnetic exchanges depending on the sign of J with the three pairs of interactions being: the nearest neighbor, next nearest neighbor and the third nearest neighbor. The isotropic Hamiltonian for this model:

$$\mathcal{H} = J_1 \sum_{(i,j)_1} S_i \cdot S_j + J_2 \sum_{(i,j)_2} S_i \cdot S_j + J_3 \sum_{(i,j)_3} S_i \cdot S_j$$

where $J < 0$ for an antiferromagnetic exchange and $J > 0$ for a ferromagnetic exchange.

Depending on the ratios between the three different spin exchange interactions $(\frac{J_2}{J_1}, \frac{J_3}{J_1})$ this model can predict long range ordered, short range order with frustrations and a gap in excitation energy, or a quantum spin liquid ground state (8).

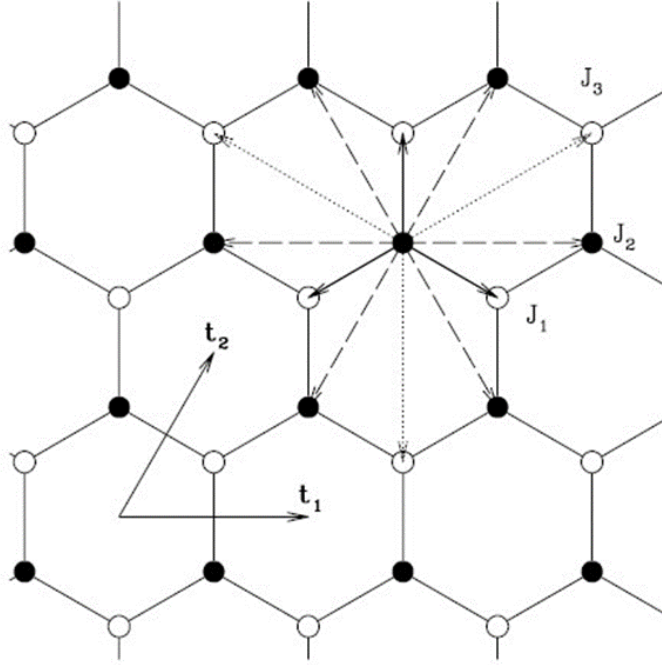


Figure 1.3: Diagram showing the three spin exchange interactions J_1 - J_2 - J_3 with solid and empty circles forming two sublattices and t_2 , t_1 are the unit cell translation vectors for a honeycomb lattice (8).

Chapter 2: Crystal Structure

2.1 Unit cell and Bravais Lattice

Crystals are distinguished from other solid states of matter by their periodic arrangement of atoms, ions, or molecules. The orientational relationships between the chemical species that make up a crystal are maintained throughout its structure. This periodic ordering can abstractly be described by a crystal lattice: an infinite array of discrete points in a line for the 1-dimensions case, a parallelogram for 2-dimensions, or a parallelepiped in 3-dimensions. The lattice is constructed by set of linearly independent translation vectors, one for each dimension, where the translation vectors are said to be primitive if they span the vector space (5). For a 3-dimensional crystal the translation vectors are $\mathbf{a}_1, \mathbf{a}_2, \mathbf{a}_3$ which are the vectors that define the crystal axes. The positions of all points in a crystal lattice (\mathbf{r}') are constructed by linear combinations of the set translation vectors: $\mathbf{r}' = \mathbf{r} + u_1\mathbf{a}_1 + u_2\mathbf{a}_2 + u_3\mathbf{a}_3$ where u_1, u_2, u_3 are integers and \mathbf{r} is an arbitrary point (5). The basis of a crystal structure is the atoms or molecules that make up composition of a crystal. The basis contains the arrangement and orientation of the crystal's constituent atoms. For each crystal there is only one basis, and each basis is associated with a single lattice point. The crystal lattice plus the basis then defines a crystal structure. The lattice points are not necessarily atomic or molecular positions, they can be at fractional sites as well so as long as they fully represented the crystals translational symmetry (11).

2.1.1 Unit cell and Bravais Lattice

The unit cell is the smallest volume that contains the full geometric description of the arrangement of constituent particles or fractions of particles that make up a crystalline solid. As such the unit can be repeated by translation operations to construct the entire crystal structure. The symmetry of a crystal defines the relationship between particles in a crystal system as well

as shape of the unit cell. There are 7 possible crystal systems in 3D (11). When the symmetrical constraints of the 7 crystal systems are combined with the particle spacing information of the crystal lattice it results in 14 possible Bravais lattices.

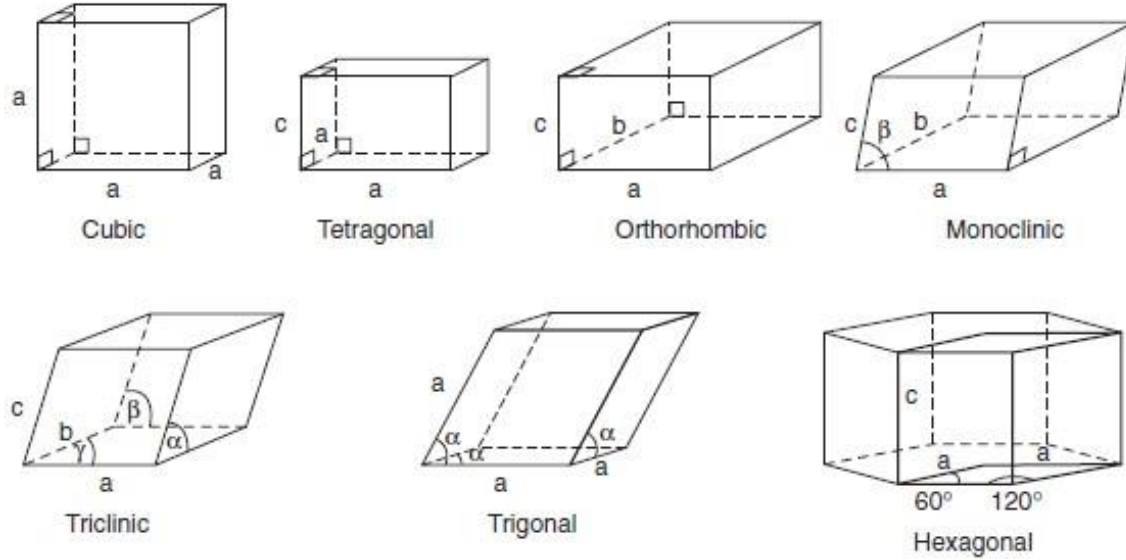


Figure 2.1: Diagrams of the seven crystal systems (11).

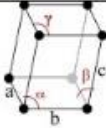
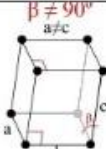
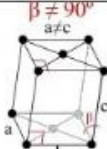
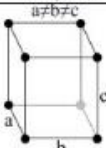

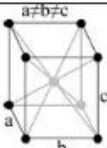

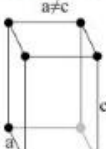
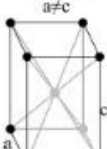
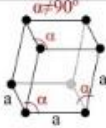
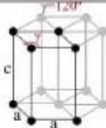
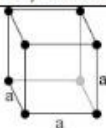
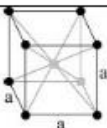

2.1.2 Reciprocal Lattice

The reciprocal lattice is the crystal lattice represented in Fourier space. Like the crystal lattice the positions of all the points of the reciprocal lattice are given by the linear combinations of the set translational vectors: $\mathbf{G} = v_1 \mathbf{b}_1 + v_2 \mathbf{b}_2 + v_3 \mathbf{b}_3$ where \mathbf{G} is the reciprocal lattice vector v_1, v_2, v_3 are integers and $\mathbf{b}_1, \mathbf{b}_2, \mathbf{b}_3$ are the reciprocal translation vectors (5). These vectors are related to the translation vectors by a Fourier transform:

$$\mathbf{b}_1 = 2\pi \frac{\mathbf{a}_2 \times \mathbf{a}_3}{\mathbf{a}_1 \cdot \mathbf{a}_2 \times \mathbf{a}_3}; \mathbf{b}_2 = 2\pi \frac{\mathbf{a}_3 \times \mathbf{a}_1}{\mathbf{a}_1 \cdot \mathbf{a}_2 \times \mathbf{a}_3}; \mathbf{b}_3 = 2\pi \frac{\mathbf{a}_1 \times \mathbf{a}_2}{\mathbf{a}_1 \cdot \mathbf{a}_2 \times \mathbf{a}_3} \quad (5).$$

The reciprocal lattice vector is an integral part of crystal diffraction as it is when the scattering vector of incident radiation is equal to a reciprocal lattice vector that the conditions for constructive interference are satisfied (5).

Table 2.1: The 14 Bravais lattice systems (12).

Lattice System	Point Group	Primitive	Base-Centered	Body-Centered	Face-Centered
Triclinic	$\bar{1}$	 $P\bar{1}$			
Monoclinic	$2/m$	 $P2/m$	 $C2/m$		
Orthorhombic	mmm	 $Pmmm$	 $Cmmm$	 $Immm$	 $Fmmm$
Tetragonal	$4/mmm$	 $P4/mmm$		 $I4/mmm$	
Rhombohedral	$\bar{3}m$	 $R\bar{3}m$			
Hexagonal	$6/mmm$	 $P6/mmm$			
Cubic	$m\bar{3}m$	 $Pm\bar{3}m$		 $Im\bar{3}m$	 $Fm\bar{3}m$

2.2 Symmetry and Space Group

Crystal systems have both point and space symmetry. For point symmetry at least one point is not affected by a symmetry operation, such as a point in which its axis is the axis of rotation for all other lattice points. In space symmetry all points are transformed under a symmetry operation. An example of space symmetry is a reflection plus a translation - a glide plane. Describing a crystal system by its symmetry reduces the need to specify all atomic position in a unit cell for a given crystal. Instead, only certain atomic positions need to be found and the remaining positions can be known by the symmetry relations of the crystal system. The total number of permutations of the 14 Bravais lattices under point and space symmetry operations yields 230 possible space groups in 3D space (11). Each space group is first labeled with a letter representing the crystal system followed by signifier letters that the represent the possible symmetry operations that define a particular space group.

Table 2.2: Crystal Systems and Symmetry (11).

Crystal system	Unit cell shape ^b	Essential symmetry	Allowed lattices
Cubic	$a = b = c, \alpha = \beta = \gamma = 90^\circ$	Four threefold axes	P, F, I
Tetragonal	$a = b \neq c, \alpha = \beta = \gamma = 90^\circ$	One fourfold axis	P, I
Orthorhombic	$a \neq b \neq c, \alpha = \beta = \gamma = 90^\circ$	Three twofold axes or mirror planes	P, F, I, A (B or C)
Hexagonal	$a = b \neq c, \alpha = \beta = 90^\circ, \gamma = 120^\circ$	One sixfold axis	P
Trigonal (a)	$a = b \neq c, \alpha = \beta = 90^\circ, \gamma = 120^\circ$	One threefold axis	P
Trigonal (b)	$a = b = c, \alpha = \beta = \gamma \neq 90^\circ$	One threefold axis	R
Monoclinic ^a	$a \neq b \neq c, \alpha = \gamma = 90^\circ, \beta \neq 90^\circ$	One twofold axis or mirror plane	P, C
Triclinic	$a \neq b \neq c, \alpha \neq \beta \neq \gamma \neq 90^\circ$	None	P

2.3 Lattice Planes

Lattice planes are imaginary planes in a unit cell that can, but not necessarily do, coincide with planes constructed from atoms or ions in a crystal. These planes divide the unit cell into fractional sections that are useful in identifying possible diffraction planes, if indeed the lattice plane represent an actual plane of particles. The orientation of lattice planes in a unit cell is given by a set of integers (hkl) that index the lattice planes, called the Miller indices (11). To derive the Miller indices for a particular plane coordinate origin is first chosen in the unit cell, typically the origin is taken to be at one the corners of the unit cell. The points along the 3-crystal axes where the lattice plane intercepts the edges of the unit cell are fractions of its 3 principal dimensions (lattice constants). The inverse of these fractions are the Miller indices. With this definition every lattice plane with same index will divide the unit cell or neighboring unit cells with same factional value of the lattice constants. Therefore, adjacent planes will be the equidistant from each other. The constant spacing between adject planes is called the d -spacing and is an important concept when viewing lattice plane as a diffraction grating for incident x-rays.

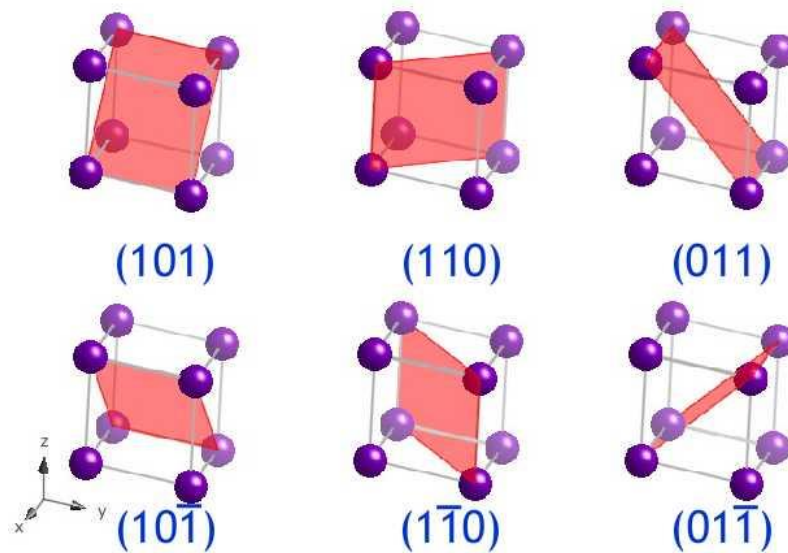
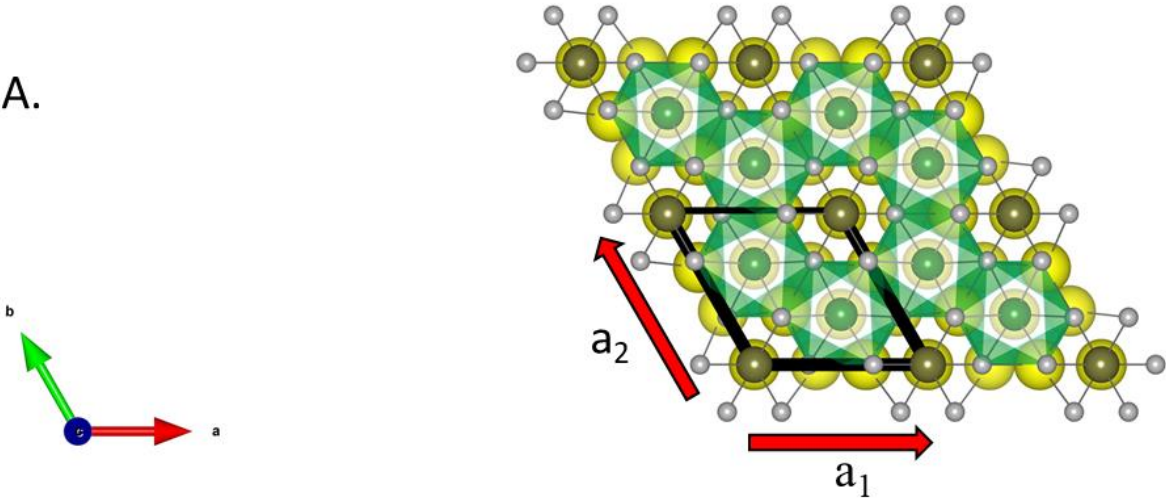


Figure 2.2: Lattice planes with Miller indices (11).

2.4 The Crystal Structure of Na₂Ni₂TeO₆

The crystal structure of most importance herein is the hexagonal close pack (HCP). HCP crystal structure consist of stacked basal plane layers with in-plane honeycomb lattice structure with interplane layers having a half hexagon lattice (11). Evstigneeva, M. A et al. (1) first identified the crystal structure of Na₂Ni₂TeO₆ to be in the P6₃/mcm space group. This space groups features 3-fold rotational symmetry, 6-fold screw axis, a glide plane along the c-axis, and a reflection through the ac plane. The d -space of HCP is given by $\frac{1}{d^2} = \frac{4}{3} \left(\frac{h^2 + hk + k^2}{a^2} \right) + \frac{l^2}{c^2}$ were h, k, l are Miller indices and a, c are lattice constants.

A.



B.

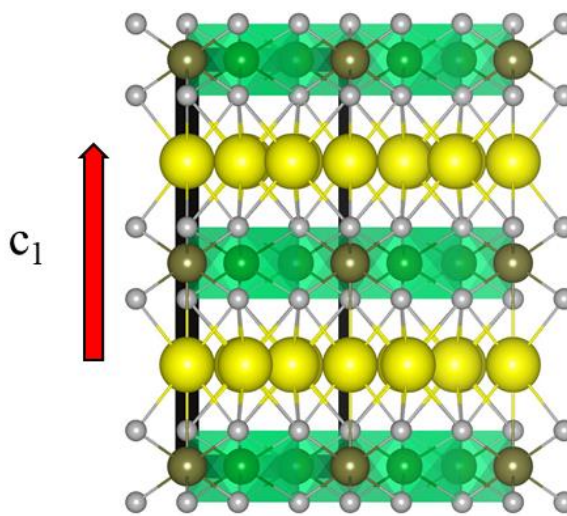
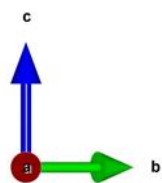


Figure 2.3: (A.) The a-b plane of $\text{Na}_2\text{Ni}_2\text{TeO}_6$ showing the hexagonal pattern of nickel cations (green spheres), and $a_1 = a_2$ lattice constants of the unit cell.
 (B.) The c-b plane of $\text{Na}_2\text{Ni}_2\text{TeO}_6$ with the c_1 lattice constant of the unit cell.

Chapter 3: Synthesis and Crystal Growth

3.1 Shake 'N Bake Method

The conventional solid-state method of materials synthesis is often colloquially referred to as the Shake 'N Bake Method. It is a direct method of materials synthesis in which the resultant product is formed by a reaction of precursor powders. To produce the precursor powder suitable reagent powders are ground in a mortar and pestle or ball mill into a bulk-level homogeneous mixture. When this mixture is subsequently calcinated it results in the formation of the target product (10).

The reactions in solid-state synthesis are carried out by an exchange of cations at the contact points between the surfaces of the polycrystalline reagents' Fig (3.1). The cationic flux is induced by the energetic favorability of the products in relation to reactants. This energy favorability is expressed as a negative change in Gibbs free energy between the product and reactants: $\Delta G = \sum \Delta G_{f \text{ products}} - \sum \Delta G_{f \text{ reactants}}$ here ΔG_f is the change in Gibbs free energy of formation given by $G_f = H - TS$ where H is the enthalpy of formation and T is temperature and S is entropy (10).

The limiting factor in solid state reactions is the flux of the cations which is described by Fick's first law of diffusion: $J_i = \sum_{ij}^N D_{ij} \frac{\partial C_i}{\partial x}$ where J_i is the Number of Atoms or Ions per unit area per unit time, D_{ij} is the Chemical Diffusion Coefficient, and $\frac{\partial C_i}{\partial x}$ is the Gradient of Concentration (10). The temperature dependence of the diffusion coefficient is given by the Arrhenius equation: $D = A * e^{-\frac{E_a}{RT}}$ here A is a Chemical Reaction Coefficient, E_a is the Activation Energy, R is the Universal Gas Constant, and T is Temperature in Kelvin (10). It is

then evident in the description of basic kinematics of solid-state reaction why it is necessary to heat the precursor powders to high temperatures. Without such a reaction rate increase provided by added thermal energy the reaction time scales would be prohibitively long (10).

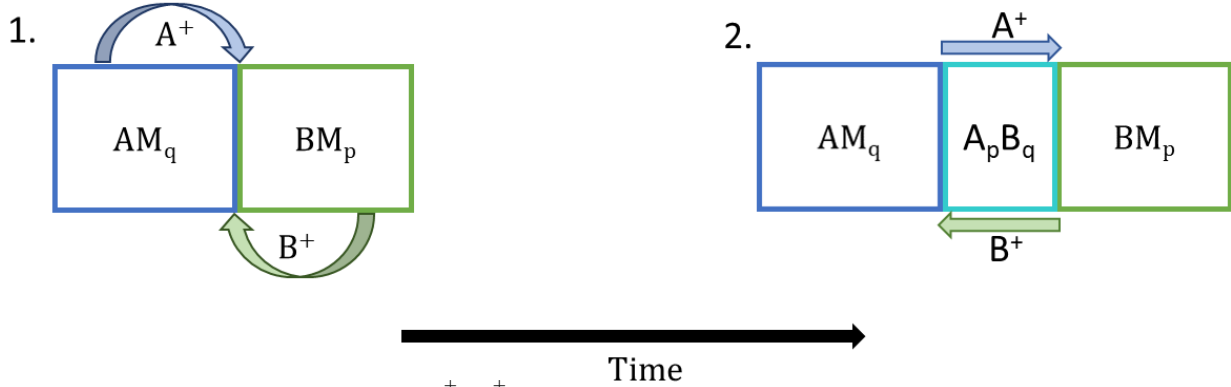


Figure 3.1: (1.) Initially cations (B^+ , A^+) are diffused through the reagents and adsorbed at crystal defect sites on the surfaces of the reagents.

(2.). After some time the product layer (A_pB_q) grows with the cations diffusing through the product towards the surfaces of the reagents. The size of the product layer is limited by the diffusion pathlength.

Crystal defects (vacancies and dislocations) play a major role in mass transport in solids. The defects provide crystal sites where cations can jump to during diffusion. Defect sites also serve as regions where the exchanged cations can be adsorbed. Local regions of adsorbed cations form sites of product nucleation in the initial stage of product formation. The following growth of the product nucleus is limited by relatively short diffusion pathlength of the cations resulting in the confinement of product formation to areas close to the nucleation centers. Diffusion pathlength r is proportional to D and time by the following relation: $r \propto \sqrt{Dt}$ (10).

In contrast to the growth rate of the nucleus, which is purely diffusion limited, the ultimate size of the nucleus has an additional limiting factor of structural stability. If the crystal lattices of the reagents and products are similar the nucleus will grow to dimensions limited to the diffusion pathlength. On the other hand, if the lattices are dissimilar stresses will develop in

the nucleus, leading to a loss of structural stability. As strain is build up in an unstable nucleus it will reach a breaking point where it will break free of its substrate. At this point the contact between reagents is lost and the reaction stops - Fig (3.2).

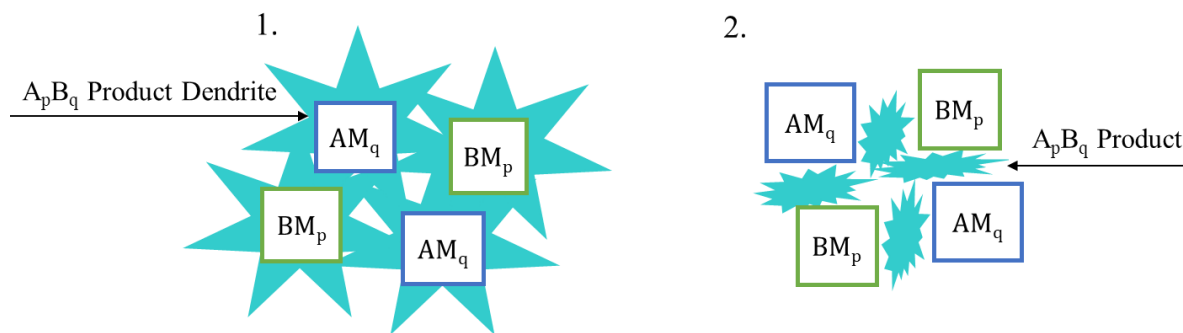


Figure 3.2: (1.) Similar crystal structure between reagents and product results in stable product growth as dendrites.
(2.) Dissimilar crystal structure of product and reagents results in unstable product growth with product layers that break away from the reagents surfaces.

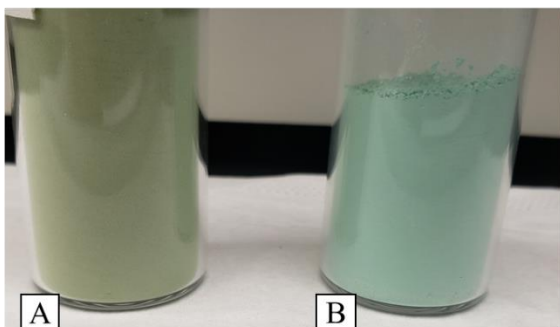
With the as described kinetics and geometric constraints of solid-state reactions in mind the reasons for steps in the Sake n' Bake method are clear. These steps are as follows:

1. Grind reagents to homogenize and reduce particle size increasing surface area or for regrinding to break up dendrites or clear off product layers.
2. Compact the ground powder increasing surface contact
3. Calcinate at high temperature ($T \geq 400^{\circ}\text{C}$) increasing cation diffusion
4. Repeat steps 1 – 3 until a pure phase of the product is achieved

3.1.2 Synthesis of $\text{Na}_2\text{Ni}_2\text{TeO}_6$

To synthesis $\text{Na}_2\text{Ni}_2\text{TeO}_6$, stoichiometric ratios of reagents (4N or higher purity the) Na_2CO_3 , NiO , and TeO_2 , purchased from Sigma Aldrich, are mixed in an agate mortar and pestle. To aide in grinding as well as ensure a homogeneous mixture, alcohol is added to the reagent powder in the mortar. This fluidizes the mixture, making it easier to thoroughly grind and mix for approximately **10 min**. Reagent grade ethyl alcohol, methanol, or acetone are often used for this purpose as these organic solvents do not contaminate the powders and evaporate quickly. Once all the alcohol has evaporated the precursor powder is pressed into pellets using a pellet pressing die in a hydraulic press using **5k PSI**. Since Na has a high pressure of evaporation when heated the pellets are first heated to a relatively low temperature of **400°C** for 30-hours with intermated regrinding and repalletizing. This step of first heating the precursor powder at a low temperature has the effect of fixing the reagents to themselves thus minimizing the loss of volatile components. It will also drive off any highly volatile contaminants such as water or any lingering organic compounds. For $\text{Na}_2\text{Ni}_2\text{TeO}_6$ low temperature initial heat cycles aids in product formation by oxidizing TeO_2 to its final oxidation state of TeO_3 (1). Then the partially reacted powder is heated to **800°C** for 24-hours with intermate regrinding and repalletizing. The chemical phase purity is confirmed by Rietveld refinement of powder x-ray diffraction data (10). For large batches, **(30 – 50) g**, a hydrostatic press is used to make rod-like compacts of the powder using a pressure of **75 MPa**. The large compacts require about **30 min** of grinding to fully break into a fine powder. To achieve a chemically pure phase for large batches an additional 12-hour heating at **800°C** is needed.

1.



2.

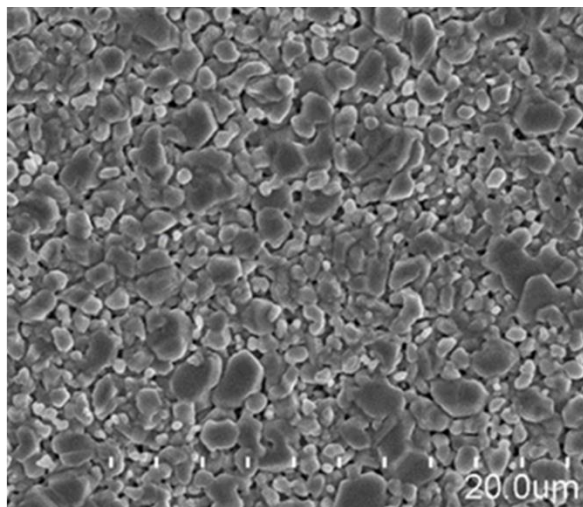


Figure 3.3: (1.) A. Precursor Powder. B. Pure Chemical Phase $\text{Na}_2\text{Ni}_2\text{TeO}_6$.
 (2.) A SEM micrograph of a sintered pellet of $\text{Na}_2\text{Ni}_2\text{TeO}_6$, grain size $\sim 5 - 20 \mu\text{m}$.

3.2 Self-Flux Melt Method of Crystal Growth

In order to make definitive experimental determination of the physical properties of a material, especially anisotropic properties, it is often necessary to have a single crystal sample. When the experiments are performed on polycrystalline powders the measured properties are an average of all contributions from the present crystallographic planes. It is particularly necessary to study single crystals when studying structurally dependent properties. This would include any anisotropic properties or properties that are low-dimensional in natural. With an orientated single crystal, the sample can be probed in a specific crystallographic direction revealing the materials directionally dependent characteristics.

The self-flux melt method crystal growth is a high temperature technique for crystal growth where the reagents that are used to produce a polycrystalline powder are used as the solvent (flux) for a pure chemical phase compound. The flux has the effect of lowering the melting temperature of the crystal powder and ensures that all the components melt congruently.

Fluxes that consist of the reagents will have the same ions as the polycrystalline powders reducing the constituents in the melt helping keep the crystals free from impurities.

The flux melt crystal growth is kinetically similar to low temperature aqueous crystal growth where the energy of crystal formation is lower than energy of the maintaining a supersaturated state. In the cases of the high temperature crystal growth the supersaturated state is induced by slowly cooling the product-rich melt. As the melted solution is cooled seed crystal will spontaneously form due to their energetic favorability. These seed crystal establish the nucleation sites that the crystals grow from (10).

To grow $\text{Na}_2\text{Ni}_2\text{TeO}_6$ crystals; the polycrystalline powder is mixed (30 g) with Na_2O (10 g) and TeO_2 (50 g) in a molar mass ratio of 1: 0.5: 2.5 (4). The mixture is placed into an alumina crucible and slowly heated to a temperature of 800°C. It is held at this temperature for 30 hours to homogenize the solution. The homogenies melt is then slow cooled using a ramp down rate of 2°C/hour to a temperature of 500°C. This slow cooling step is followed by a rapid cooling to room temperature (4).

The first crystal growth trial used the as described method which resulted in an incomplete melting of the mixture. No crystals were recovered after soaking sintered puck of $\text{Na}_2\text{Ni}_2\text{TeO}_6$ and flux in a nitric acid solution. A second trial was conducted with a substitution of NaCl for Na_2O , all other parameters remained the same. This was done to improve the meltability of the mixture as NaCl has a lower melting point than Na_2O . This trial resulted in a more complete melt, though there was still a middle section that did not fully melt using this substitution. The second trial did, however, result in the formation of a crystal fakes that were approximately 3 x 2 mm in size. Due to the poor melting the crystal yield was low and their chemical composition maybe off from the target formula.

1.



2.

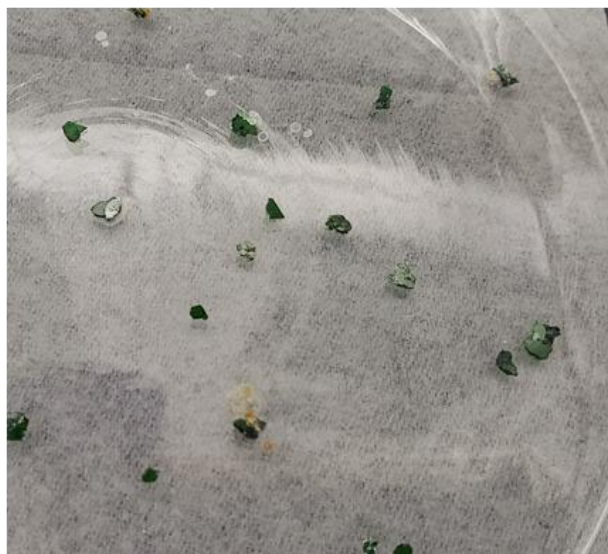


Figure 3.4: (1.) The incomplete $\text{Na}_2\text{Ni}_2\text{TeO}_6$ and flux mixture of the first trial.
(2.) Small $\text{Na}_2\text{Ni}_2\text{TeO}_6$ crystals from the second trial.

Chapter 4: X-Ray Diffraction and Neutron Scattering

4.1 Basics of Diffraction Theory and Powder Diffraction

Diffraction is the phenomenon of waves bending around an obstacle and subsequently expanding forward. Each obstacle can be viewed as a source of a new wave propagating forward in accordance with Huygens principle (11). Huygens principle imagines waves are constructed by interference of spherical waves which sum up to make a continuous wavefront. If there are several obstacles spaced at a distance similar to the incident wave's wavelength from each other, such as line of slits spaced at a wavelength from each other, the diffracted waves will interfere with each other in accordance with the superposition principle. If the interfering waves are in phase, they interfere constructively with doubling of the resultant wave's amplitude. It is the inverse for waves that are out of phase, they interfere destructively with the waves' amplitudes canceling out. The result is a diffraction pattern - a wave pattern consisting of alternating sections of increased amplitude and areas with zero amplitude (no wave).

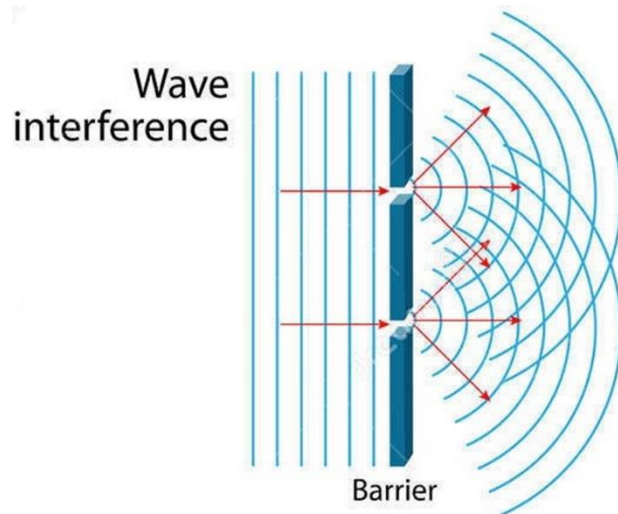


Figure 4.1: Schematic diagram of diffracted waves interfering (14).

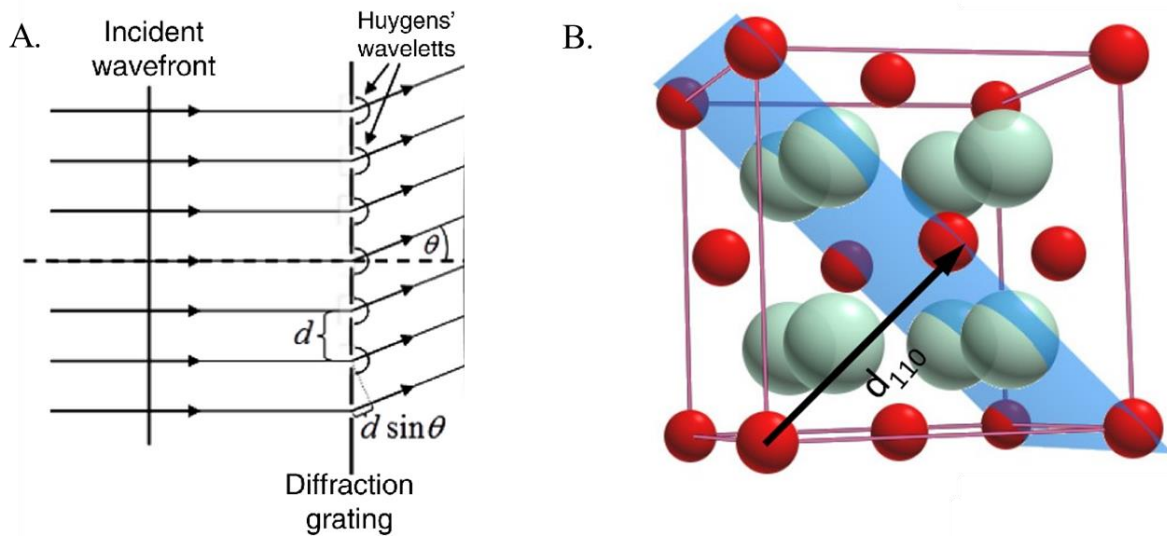


Figure 4.2: (A.) Diagram of coherent waves being diffracted by diffraction grating with slit spacing d of by an angle $d \sin \theta$ (10).
 (B.) The ordered arrangement of atoms in a crystal form planes that are a set distance (d -spacing) apart from adjacent parallel planes – producing a diffraction grating (14).

In powder crystal diffraction the planes formed by the repeating ordered arrangement of atoms serve as a diffraction grating for coherent waves. The powder diffraction pattern has information encoded in it about the crystal's microstructure. The equation that describes the conditions for waves diffracted by crystals to constructively interfere is Bragg's law:

$n\lambda = 2d \sin \theta$ where n is an integer, λ is the wavelength of the incident ray, θ is the incident angle, and d is the distance between atomic planes (5). Bragg's law is satisfied when the path length difference of two coherent waves is equal to an integer multiple of the wavelength of the incoming waves.

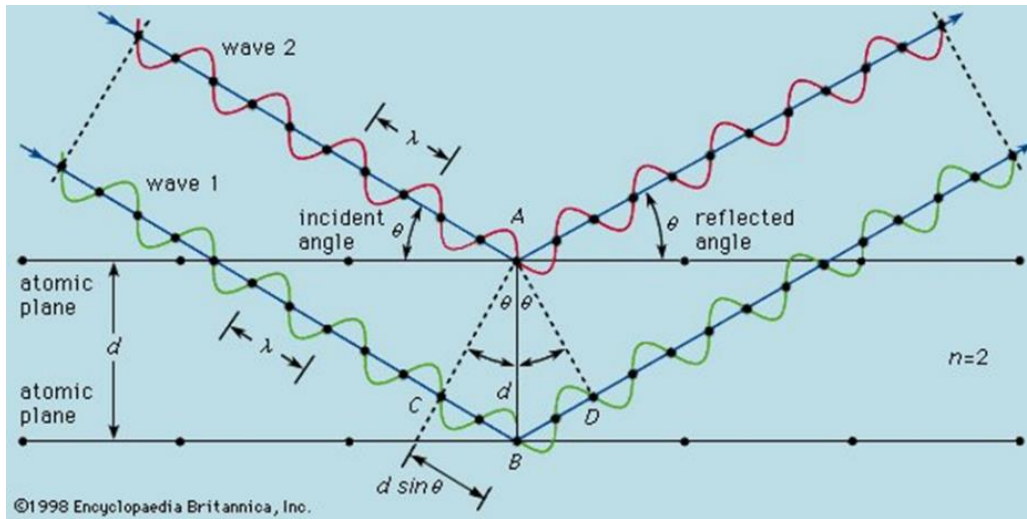


Figure 4.3: An illustration of the parameters for constructive interference of waves diffracted by adjacent atomic planes - Bragg's law. When the difference in path length ($2d \sin\theta$) is equal to an integer of the wavelength ($n\lambda$) the waves will constructively interfere (17).

Powder diffraction can be performed with particle radiation using neutrons, electrons, photons, and protons. Particles of matter, like particles of light, exhibit particle-wave duality where they have both a wave like nature and a point particle nature. The wavelength of particle of matter is given by de Broglie relation: $\lambda = \frac{h}{p}$ here λ is wavelength, h is Planck's constant, and p is momentum (13). For all crystal diffraction experiments, no matter the type of particle, there are assumptions made about the nature of the interaction of the incident beam with the crystal or the state of the polycrystalline powder. It is assumed that each particle wave will be diffracted by one atomic plane, there is zero momentum transfer (elastic diffraction), and polarization of the wave can be ignored. The result of this assumption is that all incident rays will be diffracted coherently (16). The assumptions made about the polycrystalline powder condition are those that would have the resulting diffraction be an accurate description the full crystal structure. This means that it is assumed that the powder consists of small ($\sim 20 \mu m$) crystallites, with an even distribution of all present crystal planes oriented such that the planes

will bisect the incident and diffracted rays (16). There is also assumption that a well-ground powder will be free of any set-in stress and that the surface of the powder is flat and located at the focal plane of the incoming beam. Any deviations from these ideal conditions are sources of systematic error in powder crystal diffraction experiments which will produce distortions to the diffraction pattern.

Though the wave mechanics described by Huygens principle provides a predictive model for diffraction it does not accurately describe the physics of radiation interactions with matter. What is actually happening during diffraction experiment is scattering and interference of the scattered waves, not diffraction. Scattering is the change in direction of propagation of radiation (waves or particles) by interactions with matter or by static and radiative fields (13). If there is no momentum transfer during the interactions the scattering is elastic such that the outgoing wave having the same energy as the incoming one. The scattering is inelastic if there is a momentum transfer. In terms of the wavevectors $|\mathbf{k}| = \frac{2\pi}{\lambda}$ the elastic case $|\mathbf{k}|_{Initial} = |\mathbf{k}|_{Final}$ for the inelastic case $|\mathbf{k}|_{Initial} \neq |\mathbf{k}|_{Final}$ (13). For crystal diffraction the diffraction process only serves to construct (Bragg's law) a naive model that gives the correct geometric conditions needed for waves scattered from atomic planes to interfere constructively.

4.2 Powder X-Ray Diffraction

In order for any radiation (wave or particle) to carry information about spatial features of an object the wavelength of the incident beam must be of the same order of magnitude to the feature that is to be measured. For crystals, the distances between planes of atoms (d -spacing) is in angstroms (\AA) where $\text{\AA} = 1 * 10^{-10} m$. The X-ray part of the electromagnetic spectrum has corresponding wavelengths that fit the scale of crystal d – spacing. X-rays ranging between

$\sim 1 - 100 \text{ keV}$, the energy of a quanta of light given by $E = h\nu$ and the wavelength of light $\lambda = \frac{c}{\nu}$ the range of X-ray wavelengths can be calculated using $\lambda = \frac{hc}{E}$ which results in the wavelength range of X-ray $\sim 10 - 0.1 \text{ \AA}$ (19). Scattered X-rays then can have the microstructural information of a crystal encoded in them when scattered by atoms in a crystal in powder x-ray diffraction (PXRD) experiments.

The classical electrodynamic description of electromagnetic waves being scattering by a charged particle is given by Thompson scattering (13). In applying Thompson scattering to X-ray diffraction, the electrons of the crystal's atoms interact with the incoming X-ray's oscillating electric field causing the electrons to oscillate at the same frequency as the incoming X-rays. X-rays can be mathematically expressed as a plane wave in one dimension in a vacuum so that the electric field is constant: $E(x,t) = E_0 e^{-i(k \cdot x - \omega t)}$ here E_0 is the amplitude of the wave, k is the wave number, x unit vector in the x direction, ω is angular velocity, and t is time, and i is the imaginary number (13). If the electron motion is modeled as a mass driven by the incident wave's electric field, then the electron's equation of motion will be that of a dipole oscillator: $x(t) = \frac{e}{m\omega^2} E_0 e^{i\omega t}$ where e is the charge of the electron and m is the mass of the electron. With the induced dipole moment of the electron is $p = -ex = -\frac{e^2}{m\omega^2} E_0 e^{i\omega t}$ (13). The electron dipole will radiate a new scattered wave at the same frequency as the X-rays electric field with ω and E_0 being the same value for the wave and the dipole as the collision is elastic. The result is that magnitude of wavevectors is unchanged $|k|_{incoming} = |k|_{outgoing}$ with the X-rays being scattered coherently (13).

4.2.1 Scattered X-ray Amplitudes

To calculate the amplitude of the scattered waves from a unit cell, the interference in each atom must be accounted for by an atomic form factor with conditions for elastic collisions and constructive interference account for. Then the scattered wave amplitude from the unit cell is calculated by summing over the unit cell's atomic form factors with inference between scattered waves accounted for in the summation. The amplitude of the scattered waves from an atom is proportional to the electron density and a phase factor that accounts for interatomic interference.

This amplitude is expressed in the scattering amplitude: $F = \int n(\mathbf{r}) e^{-i((\Delta\mathbf{k}) \cdot \mathbf{r})} dV$ here

$\Delta\mathbf{k} = \mathbf{k} - \mathbf{k}'$ is the scattering vector, and $n(\mathbf{r})$ is the electron concentration at position \mathbf{r} and

$\mathbf{r} = r \sin\theta$ (5). The scattering amplitude is maximized when $\Delta\mathbf{k} = \mathbf{G}$ where \mathbf{G} is a reciprocal

lattice vector. When $\Delta\mathbf{k} = \mathbf{G}$ the scattered wave interferes constructively, and Bragg's condition is satisfied. The atomic form factor for the unit cell provides the scattering amplitude factor for

the electron density of a specific atomic species in a unit cell: $f_j = \int n_j(\mathbf{r}) e^{-i(\mathbf{G} \cdot \mathbf{r})} dV$ here $n_j(\mathbf{r})$

is the electron concentration of the atom at \mathbf{r}_j (5). A simplification can be made by taking the electron density of the unit cell to be a superposition of the electron concentrations:

$n(\mathbf{r}) = \sum_{j=1} n_j(\mathbf{r} - \mathbf{r}_j)$ here $(\mathbf{r} - \mathbf{r}_j)$ is the difference between the position vector and a vector

measured at corner of a unit cell to the center of an atom \mathbf{r}_j (5). Summing the atomic form factor

over all atoms in a unit cells yields the structure factor: $S_{\mathbf{G}} = \sum_j f_j e^{-i(\mathbf{G} \cdot \mathbf{r}_j)}$ (5). The form of the

structure factor is unique for each crystal structure type. Ideal scattering intensity is given by

$S \cdot S^*$ where S^* is the complex conjugate of the structure factor S (5).

4.2.2 Powder X-Ray Diffractometers

The most common source of X-rays are X-ray tubes. X-ray tubes function by the thermal emission of electrons from a cathode held at a negative electric potential (16). The ejected electrons are accelerated towards the positive anode where they collide and release two types of radiations. When the incoming electrons collide with the electrode, they are bent by the materials atomic nucleus producing a spectrum of radiation as function of the distance the incoming electrons are from the nucleus, called bremsstrahlung. The other type of radiation is the characteristic radiation which is produced when the incident accelerated electrons collide with and knock out a low atomic orbital electron from the electrode materials atoms. When this happens, a higher orbital electron will lose energy by emitting a photon with energy in the X-ray range as it falls to fill the vacant lower orbital. The characteristic X-ray with the highest intensity is labeled $K\alpha_1$, for Cu this corresponds to a wavelength of $\sim 1.54056 \text{ \AA}$. The other characteristics wavelengths are filtered out by a Ni filter that leaves a monochromatic beam that is collimated by divergent slits (16).

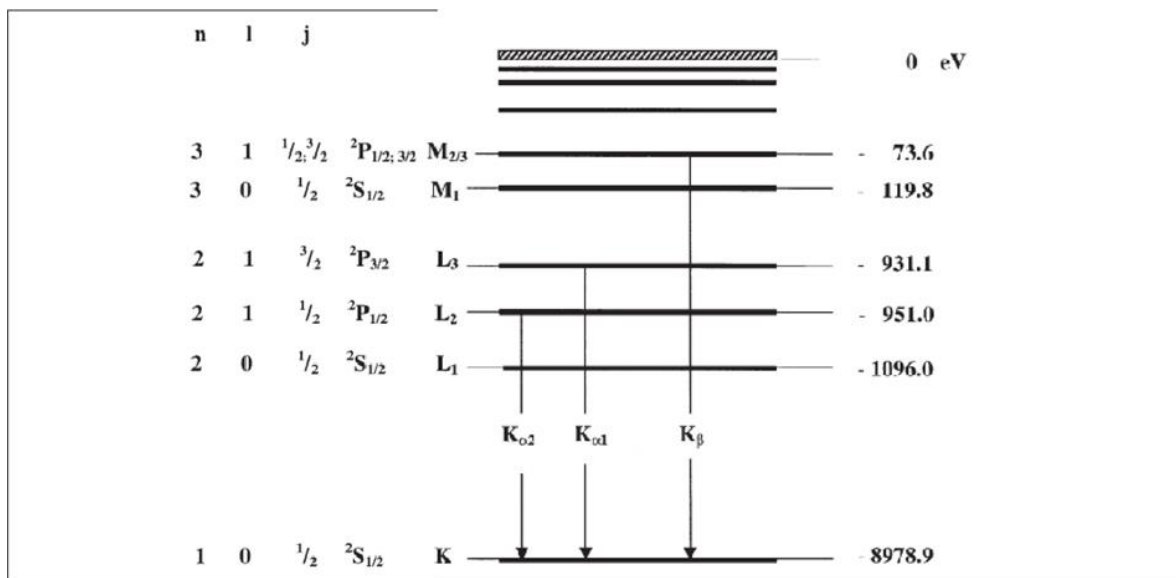


Figure 4.4: The transition of higher orbital electrons to fill the vacant orbital of an ionized Cu atom (16).

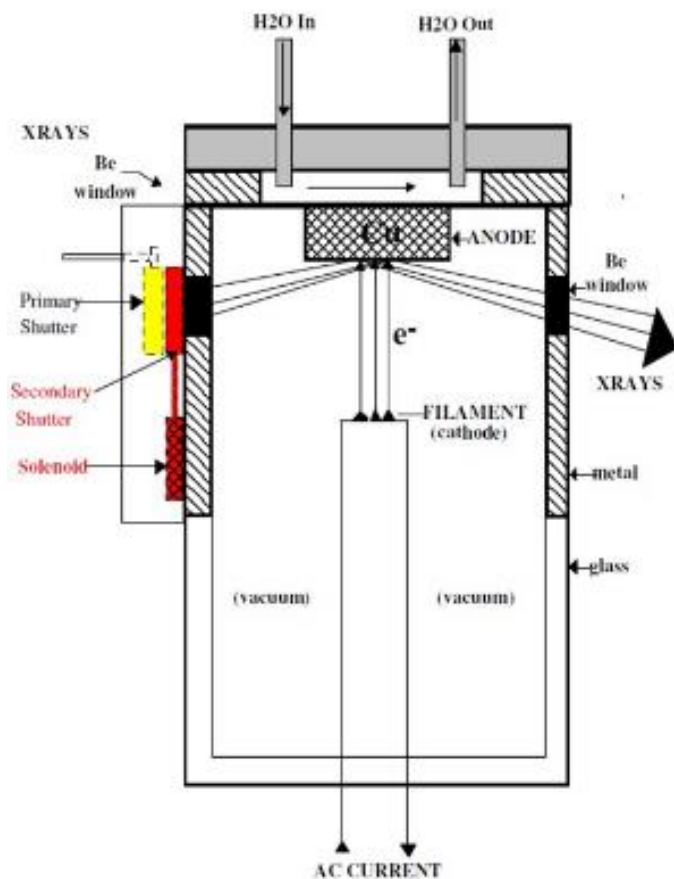


Figure 4.5: Diagram of the typical X-ray tube used in a PXRD diffractometer (16).

Laboratory diffractometers commonly operate in the Bragg-Brentano configuration to perform PXRD (16). In this configuration where the angle of the X-ray tube moves through θ and the opposing detector moves in step resulting in a measure of scattered intensity as function of 2θ

(16).

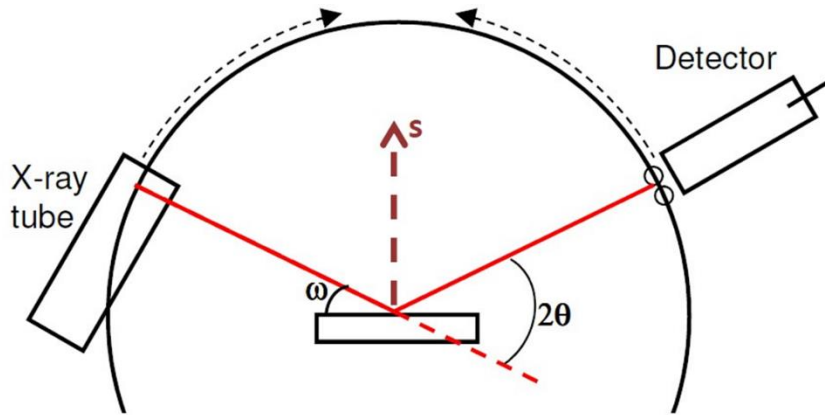
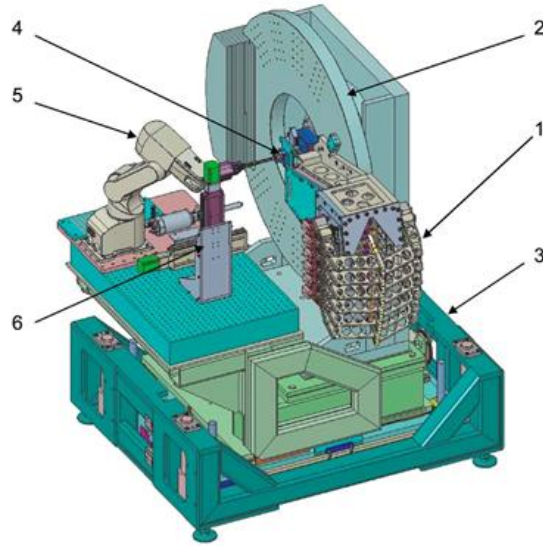


Figure 4.6: A diagram of the Bragg-Brentano configuration of PXRD with the bisecting diffraction vector \mathbf{S} kept normal to the sample surface (16).

A second source of X-rays is synchrotron particle accelerator light sources (13). These light sources can produce a wide range the wavelengths from infrared to hard x-rays. They operate by taking advantage of the fact that a charged particle moving in a curved path will emit radiation. Synchrotron X-ray sources store a current of electrons in a storage ring then use bending magnets to accelerate the circulating electrons to produce the radiation. The PXRD instrument 11-BM at the Advanced Photon Source (APS) operates with transition configuration with a wavelength range of $\sim 1.0 - 0.35 \text{ \AA}$ (21).



11-BM Diffractometer Schematic: (1) 12-analyzer detector system, (2) two-circle goniometer, (3) supporting table, (4) sample stages, (5) sample mounting robot, (6) stages for cryostream etc.

Figure 4.7: Diagram of the 11-BM Diffractometer at APS Argonne (21).

4.3 Powder Neutron Diffraction

Neutron diffraction shares the same interference conditions with X-ray diffraction but differs in the fact that neutrons interact with a material's atomic nucleus ($\sim 10^{-15} \text{ m}$) by the strong nuclear force drops of as $\frac{1}{r^3}$ as opposed to the electromagnetic interactions of PXRD that follow $\frac{1}{r^2}$ law. Also, unlike the simple linear relation of electron density with scattering amplitude, neutrons have complex interaction relationship that is isotope dependent (18). The description of neutron scattering is quantum mechanical and is given as probability of a neutron being scattered by the scattering cross section $\sigma_{total} = 4\pi b^2$ where b^2 is the scattering length that describes how a specific isotope will scatter incident neutrons (18). The scattering cross

section measured in barns (10^{-24} m^2) and the scattering length b is of the order of 10^{-15} m . The structure factor for neutron scattering is given by the correlation function: $S(\vec{q}) = \frac{1}{N} \langle \sum_{i,j=1}^N e^{i\vec{q} \cdot (\vec{R}_i - \vec{R}_j)} \rangle$ where N is the number of identical atoms and $(\vec{R}_i - \vec{R}_j)$ is the distance between nuclei (18). How neutrons scatter from a material is then given by differential scattering cross section with respect to solid angle (Ω): $\frac{d\sigma}{d\Omega} = Nb^2 S(\vec{q})$ (18). Neutrons also carry spin, which interacts with the spin of the nucleus causing incoherent scattering. If the probed material being probe contains magnetic moments, the incident neutrons will be scattered by a dipole-dipole interaction. The scattering of neutrons by the periodic arrangement of magnetic moments endows neutron diffraction the same ability to probe the magnetic structure of a material as scattering from the nucleus probes the crystal structure. Magnetic neutron scattering is described by an ion specific magnetic form factor (18).

Neutron diffraction utilizes thermal neutrons with energies in the range of $10 - 100 \text{ meV}$ giving a range of wavelengths of $3 - 0.9 \text{ \AA}$ given by the De Broglie relation $\lambda = \frac{h}{mv}$ (18). There are two sources for these cold neutrons: nuclear reactors, and spallation sources. A nuclear reactor in its self-sustaining or critical state produces about 2.5 free neutrons per reaction. The free neutrons are thermalized by the reactor's cooling water and can be diverted to diffraction instruments using beam tubes. The range of neutron energies form a Lorentzian distribution (18). For use in a diffractometer the distribution of wavelengths is spatially distributed by a monochromator. A single wavelength is then selected for diffraction experiments. The high-resolution powder diffractometer (BT-1) the National Institute for Standards and Technology (NIST). BT-1 can operate using 3 different monitors with each of the

crystal monochromators selecting a different wavelength of either (2.079Å, 1.540Å, 1.197Å) (30).

4.4 Rietveld Refinement

A PXRD pattern is made up from many contributing factors that all influence diffraction peak profile or diffraction peak position. These factors include the crystal structure and atomic properties of the material being measured, the instrument parameters, and all the sources of systematic error. To deal with convolution of factors that sum to produce a diffraction pattern Dutch physicist Hugo Rietveld produced a method of analyzing the whole diffraction pattern using least squares regression analysis (21). In the Rietveld PXDR refinement, all the contributing factors are considered in a theoretical model that the experimental data is compared to. These factors are systemically varied (refined) to produce an optimized fit of the theoretical pattern to the experimental pattern - in doing so the parameters are deconvoluted.

The equation to be minimized in Rietveld refinement is the weighted non-linear least squares equation: $M = \sum_i w_i (I_i^{obs} - I_i^{calc})^2$ where $w_i = \frac{1}{I_i^{obs}}$ the experimental recorded intensity is ; I^{obs} , and I^{calc} is the theoretical intensity (21). For a powder diffraction pattern with a single chemical phase is given by: $I_i^{calc} = S_F \sum_{k=1}^{N_{peaks}} L_k |F_k|^2 (2\theta_i - 2\theta_k) P_k A + bkg_i$ here S_F is the beam intensity, L_k = the Lorentz-polarization factor, F_k = structure factor, $(2\theta_i - 2\theta_k)$ = profile shape function, P_k = preferred orientations parameter, A = the absorption, bkg_i = background that is either modeled by a polynomial or taken as points in the pattern that represent the background noise (21). A measure of the quality of the refinement is given by the weighted profile residual: $R_{wp} = \sqrt{\frac{\sum_i^N [w_i (I_i^{obs} - I_i^{calc})]^2}{\sum_i^N [w_i I_i^{obs}]^2}}$ and the expected profile

residual: $R_{exp} = \sqrt{\frac{(N-p)}{\sum_i^N [w_i I_i^{obs}]^2}}$ here $w_i = \frac{1}{\sqrt{I_i^{obs}}}$ and P is the number of parameters and N is the

number of points (21). How well the refined calculated pattern models the experiment data, the

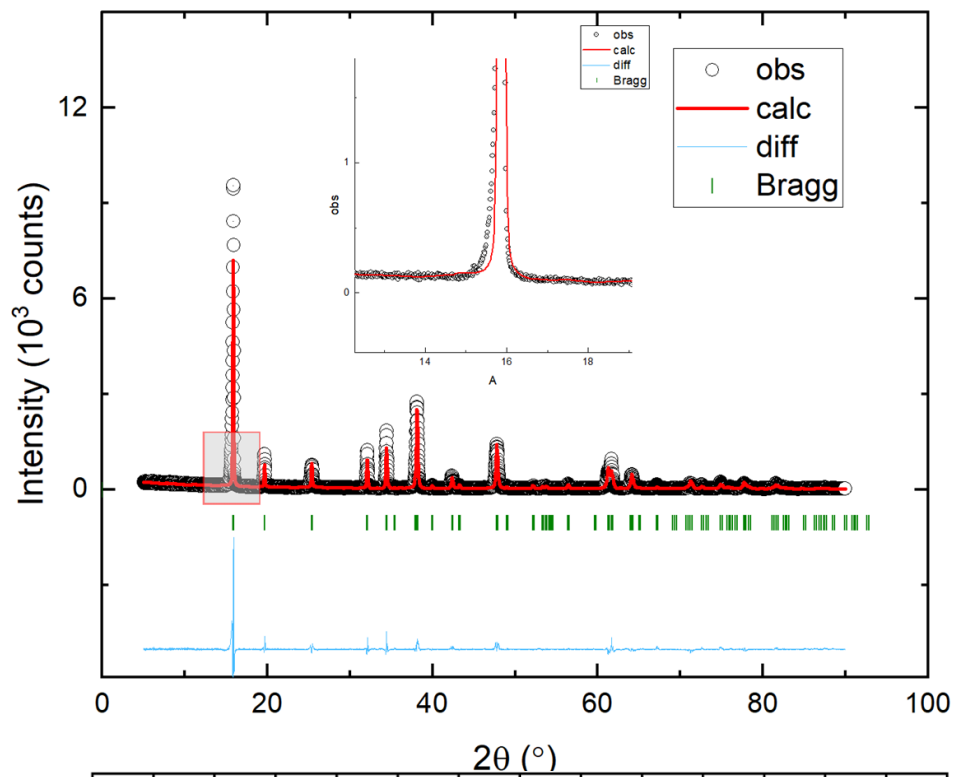
goodness of fit, is given by the ratio of the residuals: $\chi^2 = \frac{R_{wp}}{R_{exp}}$. There is no non-arbitrary value

for χ^2 that defines a well refined PXRD pattern, but it is often taken that value of $\chi^2 < 5$ represent a well PXRD parameters (22).

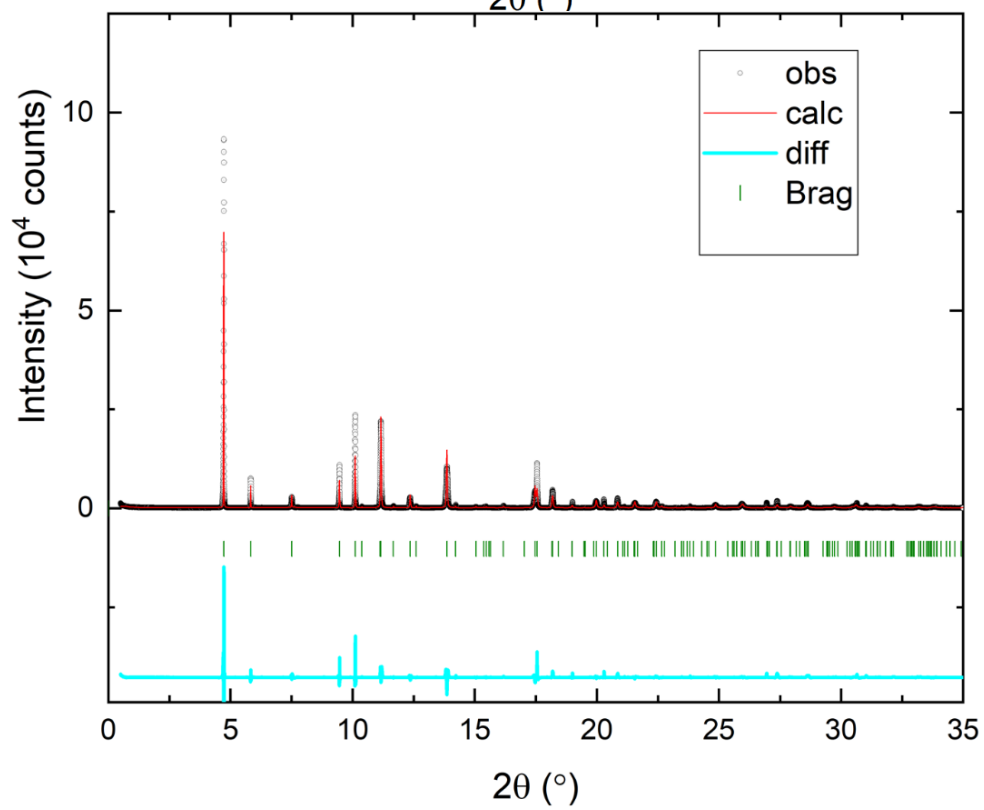
4.4.1 Rietveld Refinement of Powder X-Ray and Neutron Diffraction data For Na₂Ni₂TeO₆

Na₂Ni₂TeO₆ refines well in the *P6₃/mcm* and atomic positions with three Na sites that was first reported in reference (1). Difficulties arise in refining this compound due to stacking faults that are common in HCP materials (4). Stacking faults show up in the diffraction pattern as asymmetric peak broadening that is not well handle by whole model fitting like Rietveld refinement. This results in Na₂Ni₂TeO₆ having a high goodness of fit (χ^2), which is most apparent when trying to refine high resolution PXDR data.

A.



B.



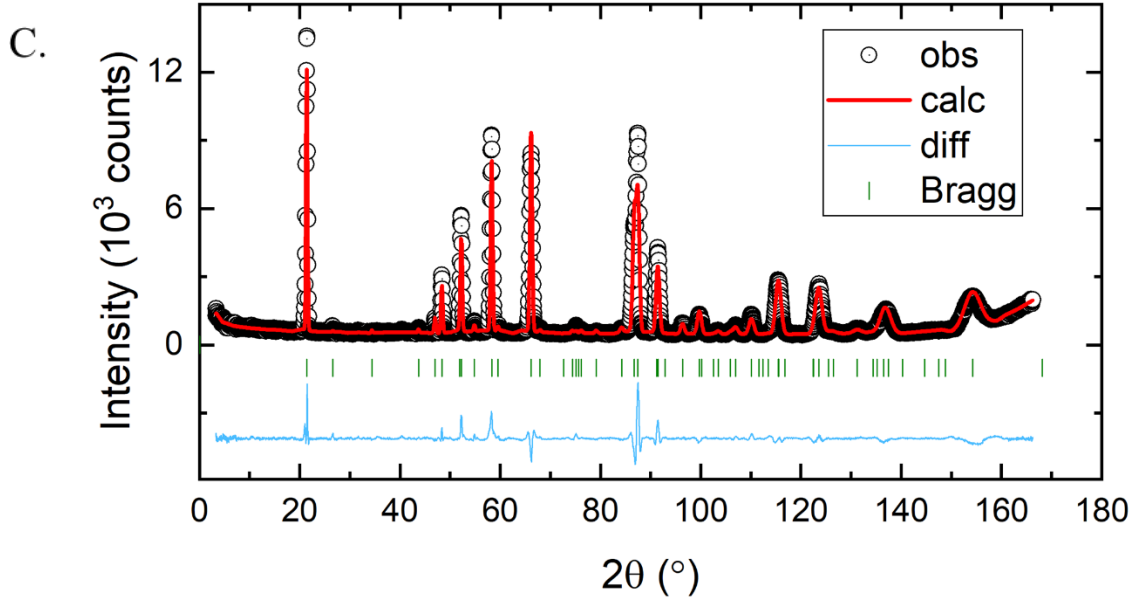


Figure 4.7: Graphs of Rietveld refinement (FullProf) of powder diffraction data for $\text{Na}_2\text{Ni}_2\text{TeO}_6$ measured on three different diffractometers.

A. Laboratory PXRD (Inset shows zoom-in lower portion of first peak)

B. Synchrotron light source PXRD ($T = 100\text{ K}$)

C. High resolution neutron powered diffraction ($T = 295\text{ K}$)

The Rietveld refinement plots of $\text{Na}_2\text{Ni}_2\text{TeO}_6$ consist of black circles (obs) that are the experimental powder diffraction data, the red line is the calculated diffraction pattern (calc), the blue line (diff) is the fitting residual, and the green ticks (Bragg) are the calculated Bragg positions. Laboratory PXRD was performed on a PANalytical p-xrd Empyrean 2 at room temperature using spinning sample stage, 16 mm slide, 30 min measurement time, and a copper X-ray source with a wavelength of 1.54 Å. The synchrotron PXRD was performed at the Advanced Photon Source using 11-BM beam line with a wavelength of 0.487897 Å at 295 K. High resolution neutron diffraction data experiments were conducted using the instrument BT-1

at NIST Center for Neutron Research, utilizing neutrons a wavelength of 2.0772 \AA . Two temperatures for neutron diffraction were used to study $\text{Na}_2\text{Ni}_2\text{TeO}_6$, $T = 295 \text{ K}$ to probe the nuclear structure and $T = 5 \text{ K}$ which is below the magnetic transition temperature ($T_N \approx 27 \text{ K}$) to look at the magnetic structure.

$\text{Na}_2\text{Ni}_2\text{TeO}_6$ refines well in the $P6_3/mcm$ space group and using the atomic positions with Wyckoff labels listed in table 4.1 as a starting model for refinement (3). The refinement is kept from reaching an optimal low value for goodness of fit by asymmetries of the observed peak profiles – inset of graph (A). These asymmetries are due to stacking faults in the layers of hexagonal close packed strutter of $\text{Na}_2\text{Ni}_2\text{TeO}_6$. Stacking faults are not well modeled by whole profile fitting and need to be modeled separately.

Table 4.1 list the atomic positions with Wyckoff labels, and B_{iso} values from the results of the Rietveld refinement performed on high resolution neutron diffraction data at two measurement temperatures. The refinement was performed using the FullProf software suite. From the nuclear diffraction data collected at the lattice constants refined are $a = b = 5.2023(2) \text{ \AA}$; $c = 11.1433(9) \text{ \AA}$ for $T = 295 \text{ K}$ data, and $a = b = 5.1955(6) \text{ \AA}$; $c = 11.1008(5) \text{ \AA}$ for $T = 5 \text{ K}$ data.

Table 4.1: Refined atomic positions of $\text{Na}_2\text{Ni}_2\text{TeO}_6$ at 295 K and 5K refined from neutron data obtained from BT-1 instrument.

Atom ($T = 295\text{ K}$)	x	y	z	B_{iso}
Te(2a)	0.0	0.0	0.0	0.19
Ni(4c)	$\frac{2}{3}$	$\frac{1}{3}$	0.0	0.30
O(12b)	0.3112(3)	0.3112(5)	0.0	0.57
Na1(6g)	0.6306(7)	0.0	$\frac{1}{4}$	0.50
Na2(4c)	$\frac{1}{3}$	$\frac{2}{3}$	$\frac{1}{4}$	0.20
Na(2a)	0.0	0.0	$\frac{1}{4}$	0.73
Atom ($T = 5\text{ K}$)	x	y	z	B_{iso}
Te(2a)	0.0	0.0	0.0	0.19
Ni(4c)	$\frac{2}{3}$	$\frac{1}{3}$	0.0	0.30
O(12b)	0.6852(4)	0.6852(3)	0.0	0.57
Na1(6g)	0.3700(2)	0.0	$\frac{1}{4}$	0.50
Na2(4c)	$\frac{1}{3}$	$\frac{2}{3}$	$\frac{1}{4}$	0.20
Na(2a)	0.0	0.0	$\frac{1}{4}$	0.73

4.5 Solving the Magnetic Structure Using SARAh

The arrangement of magnetic moments in a crystal lattice forms a periodic structure of its own, the magnetic structure. Magnetic structure is defined by a propagation vector $\mathbf{k}(\alpha^*, \beta^*, \gamma^*)$ which is a three-component vector in reciprocal space (22). The simplest magnetic structures can be described by a single \mathbf{k} - *vector* while complicated structures require multiply \mathbf{k} - *vectors*

to fully capture the symmetries of the structure. There are two types of propagation vectors, commensurate which have a periodicity which is a rational multiple of the lattice and incommensurate that are irrational. The general magnetic structure is given a Fourier series:

$m_{ij} = \sum_k \psi_j^k e^{-2\pi i k \cdot t}$ where t is the crystallographic translation vector and ψ_j is a Fourier coefficient with $\psi_j = \sum_v C_v \psi_v$ and the v indexing the components of the propagation vector k (22).

The software program SARAh uses the symmetry elements (points, lines, planes) of the Brillouin zone before the magnetic transition to generate a set a set of trial propagation vectors (22). These trial vectors are then evaluated using a reverse-Monte Carlo algorithm that takes account of the magnetic moment orientations at their crystallographic sites (22). The sorted k vectors for a particular nuclear space group as per the symmetry conditions are then systemically checked by performing a Rietveld refinement in FullProf by an adding it as an additional phase. The magnetic structure of a compound is then described by the set of propagation vectors that results in the best fit to the powder neutron diffraction data that includes the magnetic contribution to the diffraction peaks.

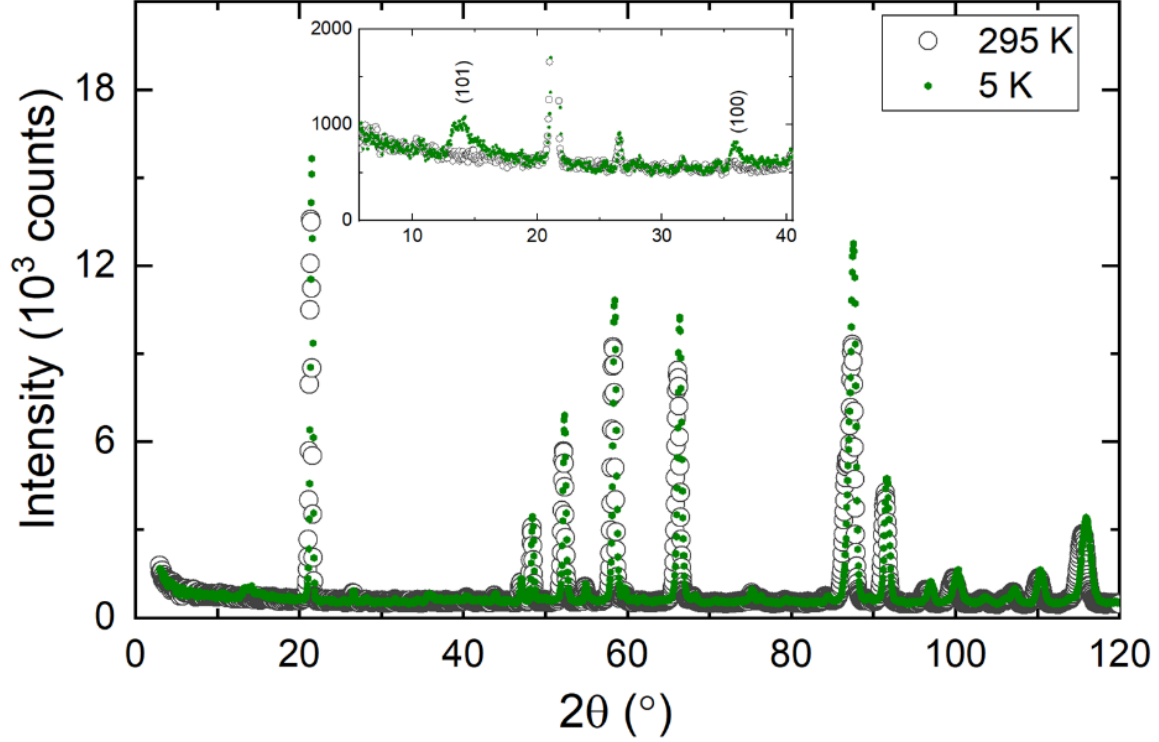


Figure 4.8: The neutron diffraction patterns above the magnetic transition temperature (black circles) and below the transition (green dots), the inset shows a zoomed in portion of plots where two magnetic peaks in the 5 K data are present.

4.5.1 The Magnetic Structure of $\text{Na}_2\text{Ni}_2\text{TeO}_6$

The first reported analysis of the magnetic structure of $\text{Na}_2\text{Ni}_2\text{TeO}_6$ proposed two propagation vectors, a commensurate vector $k_c = (0.5 \ 0 \ 1)$, and an incommensurate vector $k_{ic} = (0.47 \ 0.44 \ 0.28)$, though they did not report any Rietveld refinement using these vectors (3). Another study on the same compound using polarized neutrons showed evidence short-range diffuse magnetic order (23). Evidence for short range is also indicated by the broad magnetic peaks in the low 2θ range, around 14° and 34° , in the 5 K BT-1 neutron diffraction pattern (Fig 4.8). A k -search in SARAh yields eight irreducible representations of the magnetic structure:

$\Gamma_{mag} = \Gamma_1 + \Gamma_2 + \Gamma_3 + \Gamma_4 + \Gamma_5 + \Gamma_6 + \Gamma_7 + \Gamma_8$. A more recent study using the same set of basis vectors analyzing using Rietveld model fitting and taking account of crystal symmetry identified three different propagation vectors $k_c = (0.5 \ 0 \ 0)$, $k_c = (0 \ 0.5 \ 0)$, and $k_c = (0.5 \ 1 \ 0.5)$ describing the same magnetic structure but with different orientations. They also noted that the incommensurate vector $k_{ic} = (0.47 \ 0.44 \ 0.28)$ did not faithfully fit the observed broad peaks, around 14° and 34° (24). The resultant magnet structure represented by these vectors consists of in-plane 2D ferromagnetically order zig-zag chains (shown in Fig 4.9) that are antiferromagnetically order to adjacent zig-zag chains (24). This study did not include a model of the observed short-range order (24). To obtain the best fitting magnetic phase for $\text{Na}_2\text{Ni}_2\text{TeO}_6$ we systemically analyzed four different models of the magnetic phase added to the nuclear structure model in our Rietveld refinements. The first model tried was used the commensurate vector $k_c = (0.5 \ 0 \ 1)$, and incommensurate vector $k_{ic} = (0.47 \ 0.44 \ 0.28)$, resulting a goodness of fit of $\chi^2 = 7.3$. Using propagation vector of $k_c = (0.5 \ 0 \ 0)$ for the magnetic phase representation resulted in relatively poor a goodness of fit of $\chi^2 = 8.4$. Adding a second magnetic phase with $k_c = (0.5 \ 0 \ 0.5)$ improved the refinement giving a goodness of fit of $\chi^2 = 7.7$, however the broad peaks were still not well accounted for by this model. The best fitting model incorporated a Lorentzian peak shape model for short-range order along with the two previous propagation vectors. The resulting goodness of fit with the two magnetic phases and short-range magnetic order was $\chi^2 = 6.8$. The estimated magnetic structure described by the two magnetic phases is quasi-2D with nearest neighbor Ni^{+} magnetic moments ferromagnetically

aligned on the honeycomb superlattice and antiferromagnetically aligned with next nearest neighbor Ni^{2+} moments.

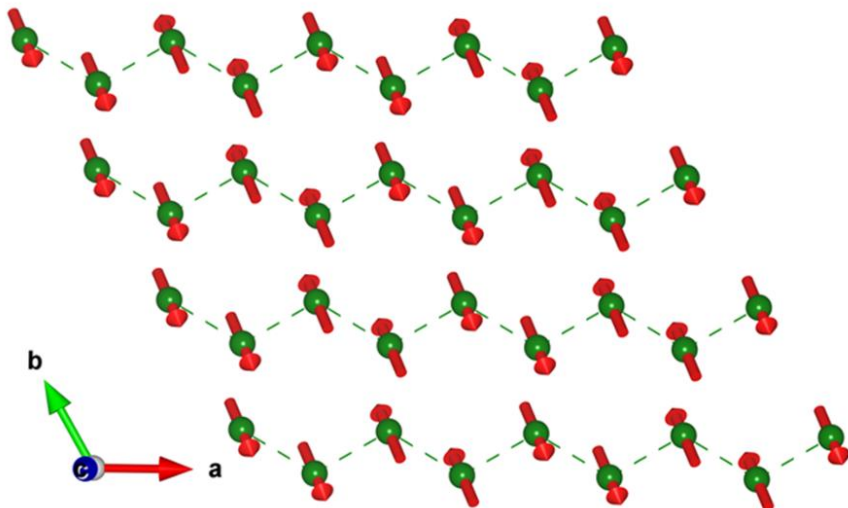


Figure 4.9: Ni cations on a honeycomb lattice (green spheres) with the magnetic moments (red arrows) arranged in zig-zag ferromagnetic chains that are antiferromagnetically aligned with each other. The magnetic structure is determined from the neutron diffraction data on $\text{Na}_2\text{Ni}_2\text{TeO}_6$ at 5K obtained from BT-1 instrument.

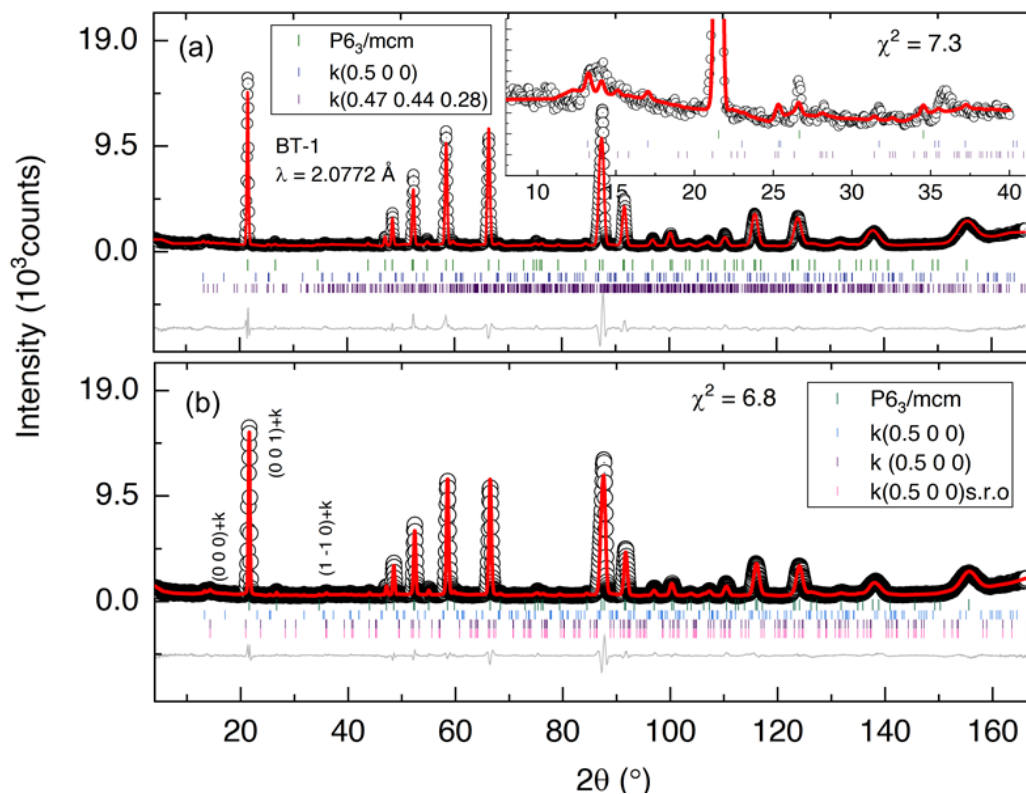


Figure 4.10: (a) The Rietveld refinement plot of $\text{Na}_2\text{Ni}_2\text{TeO}_6$ neutron diffraction data at $T = 5K$ obtained from BT-1, incorporating nuclear structure in the $P6_3/mcm$ space and two-phase magnetic model with a commensurate $\vec{k}_c(0.5 \ 0 \ 0)$ and incommensurate $\vec{k}_{ic}(0.47 \ 0.44 \ 0.28)$ propagation vectors.

(b) The Rietveld refinement plot of $\text{Na}_2\text{Ni}_2\text{TeO}_6$ neutron diffraction data at $T = 5K$, incorporating nuclear structure in the $P6_3/mcm$ space and two-phase magnetic model with commensurate propagation vectors $\vec{k}_c(0.5 \ 0 \ 0)$ and $\vec{k}_c(0.5 \ 0 \ 0.5)$ and short-range order.

Table 4.2: A table of the four magnetic structure models used for the analysis of neutron diffraction pattern at $T = 5K$. The fitting residuals are tabulated, R_p , R_{wp} , R_B , R_{mag} , to provide quantitative comparison of the four models.

Model	Phase	R_p	R_{wp}	R_B	R_{mag}	χ^2
Model 1	$P6_3/mcm + \vec{k}_c(0.5 \ 0 \ 0) + \vec{k}_{ic}(0.47 \ 0.44 \ 0.25)$	6.3	8.4	5.6	35.6, 23.9	7.3
Model 2	$P6_3/mcm + \vec{k}_c(0.5 \ 0 \ 0)$	6.5	8.9	5.5	80.5	8.4
Model 3	$P6_3/mcm + \vec{k}_c(0.5 \ 0 \ 0) + \vec{k}_c(0.5 \ 0 \ 0.5)$	6.3	8.5	5.2	66.2 54.3	7.7
Model 4	$P6_3/mcm + \vec{k}_c(0.5 \ 0 \ 0) + \vec{k}_c(0.5 \ 0 \ 0.5) + s.r.o$	6.0	8.2	4.9	42.2, 39.2, 27.4	6.8

4.6 Inelastic Neutron Scattering

Inelastic neutron scattering is a spectroscopic technique that provides information of the dynamic response of material that are accessible by an energy transfer interaction with incident neutrons (18). The scattered neutrons interacted with a material's atomic nucleus in the crystal structure (phonons), and the magnetic structure (magnons). This allows inelastic neutron scattering the ability to probe atomic motions and collective excitations present in a material.

Unlike diffraction the magnitude of the incoming and outgoing neutron wavevector is not equal

$|\vec{k}|_{incoming} \neq |\vec{k}|_{outgoing}$. Resolving the energy transfers at a resonant energy provides descriptive information of atomic motions and elementary excitations (18). Inelastic neutron scattering can probe a material's momentum space by fixing the incident neutrons energy and

scanning through continuum of Q values were $Q = \frac{2\pi}{d} \text{ \AA}^{-1}$, or the excitation energies by fixing Q and scanning through continuum of incident neutron energies (18).

A common type of inelastic neutron scattering instrument is a triple axis spectrometer which has three axes of rotation (18). Triple axis spectrometers utilize a large rotating drum that selects a fixed incident neutrons energy by rotating to an angle corresponding to the energy of the neutrons that have been spatially dispersed by the instrument's monochromator crystal. The second axis is the rotation axis of the sample and the third axis fixes the final energy of the scattered neutrons by rotating its analyzer crystal to corresponding to the desired neutron wavelength. Triple axis neutron spectrometers use a constant wavelength neutron source (18).

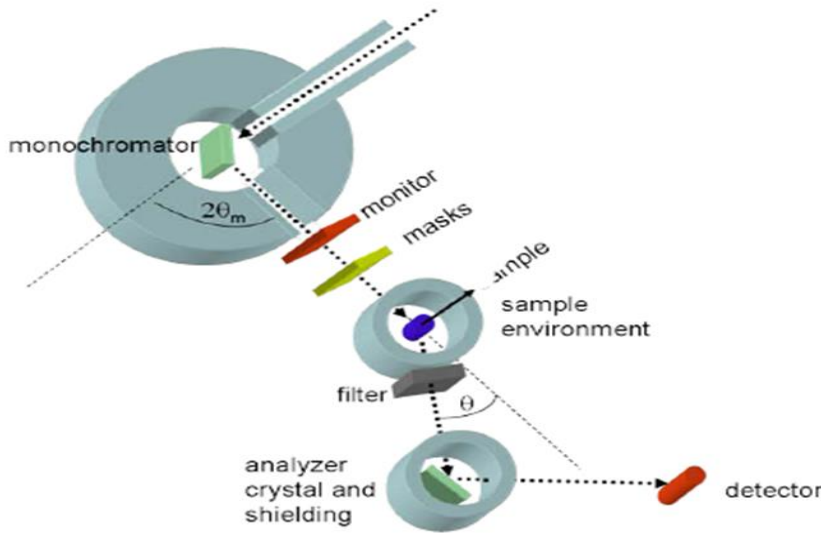


Figure 4.11: A schematic of a triple axis neutron spectrometer (18).

4.6.1 Inelastic Neutron Scattering of $\text{Na}_2\text{Ni}_2\text{TeO}_6$:

Inelastic neutron scattering was performed at University of Missouri Research Reactor Center using the instrument Triax (18). Constant Q scans were conducted at two temperatures below the T_N temperature for $\text{Na}_2\text{Ni}_2\text{TeO}_6$, $T = 5 \text{ K}$ and $T = 20 \text{ K}$. The results of the 5 K and

20 K scans show a clear extinction peak at $\approx 4.5\text{ meV}$ for three Q values $0.75\text{ \AA}^{-1}, 0.98\text{ \AA}^{-1}, \text{ \AA}^{-1}$. At $Q = 0.89\text{ \AA}^{-1}$ the excitation peak for is at energy of $E = 4.52(6)\text{ meV}$ with a full-width-at-half-maximum, $FWHM = 1.87(7)\text{ meV}$, and at 20 K for the same $Q = 0.89\text{ \AA}^{-1}$ the peak is centered at $E = 3.05(7)\text{ meV}$ with the same $FWHM$ as the 5 K peak. For a value of $Q = 2.09\text{ \AA}^{-1}$ at $T = 5\text{ K}$ there are two major excitation peaks observed with centers at $E = 4.8(3)\text{ meV}$, and $E = 8.65(5)\text{ meV}$.

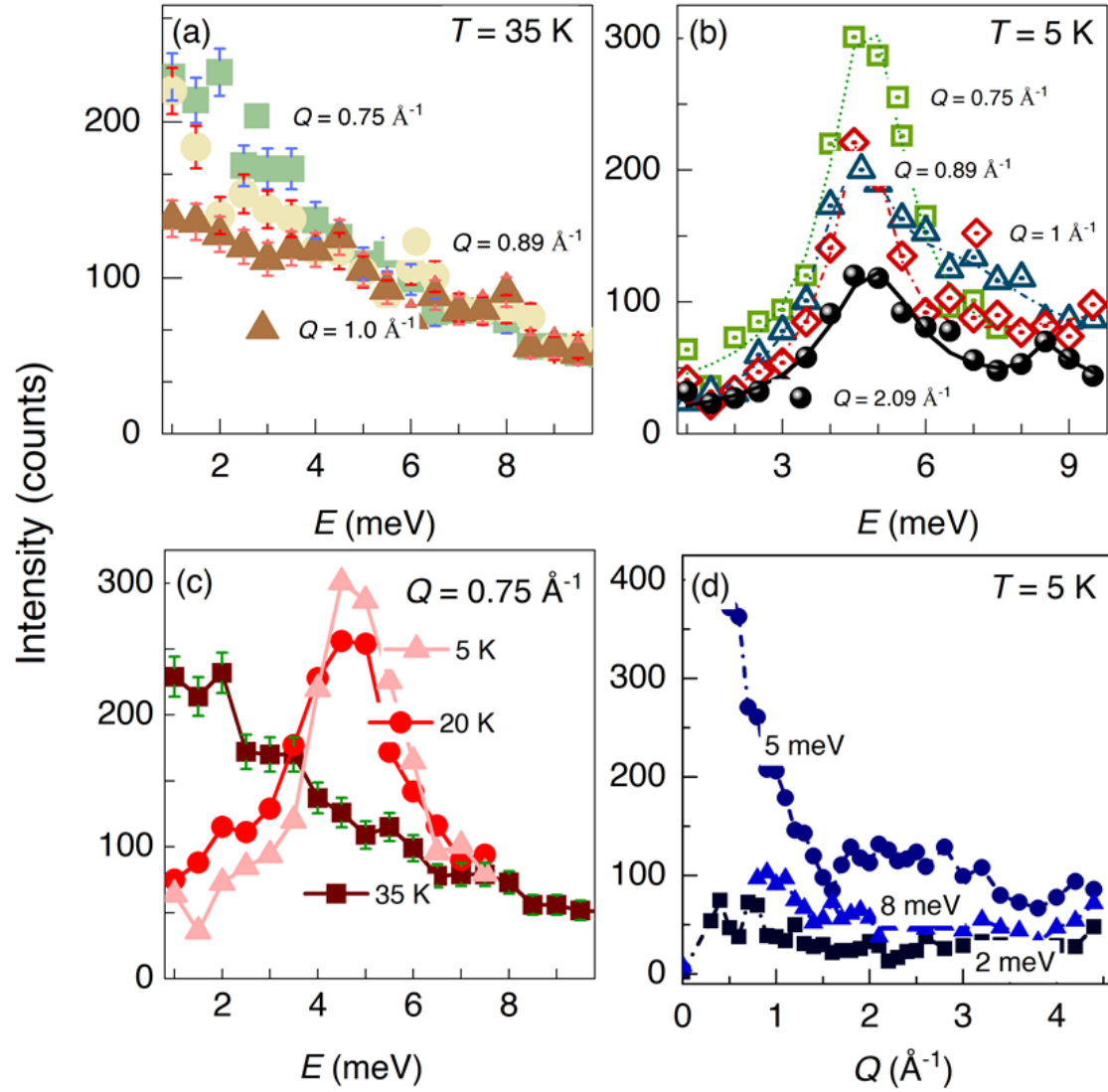


Figure 4.12: (a) Intensity of inelastic scattered neutrons at $T = 35 \text{ K}$ for three Q - values: 0.75 Å^{-1} , 0.89 Å^{-1} , and 1.0 Å^{-1} . (b) Intensity of inelastic scattered neutrons at $T = 5 \text{ K}$ for three Q - values: 0.75 Å^{-1} , 0.89 Å^{-1} , 1.0 Å^{-1} , and 2.09 Å^{-1} , dashed lines are standard profile fits. (c) Constant- Q (0.75) E -scan at 5 K , 20 K , and 35 K . (d) Q - dependence of intensity at 5 K for $E = 2 \text{ meV}$, $E = 5 \text{ meV}$ and $E = 8 \text{ meV}$.

Chapter 5: Bulk Properties of Na₂Ni₂TeO₆

5.1 Specific Heat Capacity

Specific heat capacity of a material is the amount thermal energy (∂Q) a material absorbs in response to the change of temperature (∂T) of its environment per unit mass (m): $C = \frac{\delta Q}{m \delta T}$.

For a constant pressure process specific heat capacity is the differential of enthalpy:

$$C_p = \left(\frac{\delta Q}{m \delta T} \right)_p = dh = du + P dv = \frac{\delta h}{\delta T} \text{ (J} \cdot \text{K}^{-1} \cdot \text{Kg}^{-1}) \text{ where } u \text{ is internal energy per unit}$$

mass, P is pressure and v is volume per unit mass (25). Since heat capacity is a thermodynamic property it depends on the state of the system as well as the physical properties of the material such as bond strength and magnetization. One of thermodynamic properties that dictates the heat capacity of a material is entropy. Entropy is the measure of the randomness or uncertainty in the motion of atoms and molecules. Entropy is given by the summation of the probabilities of the particles in a system to be in a particular microstate: $S = -k_B \sum_i p_i \cdot \log(p_i)$ where k_B is the Boltzmann constant and p_i is the probability of beginning in a particular state (25). Entropy is then dependent on the degrees of freedom that define the system's microstates. For magnetic degrees of freedom entropy is given by: $S_{mag} = 2R \ln(2S + 1)$ where R is the universal gas constant and

S is spin (4). The degrees of freedom and their associated energies set a material's entropy and therefore its heat capacity by the following relation: $C_p = T \left(\frac{\delta S}{\delta T} \right)_P$ here T is temperature S is

entropy and P is pressure (25).

5.1.2 Specific Heat Capacity of $\text{Na}_2\text{Ni}_2\text{TeO}_6$

The specific heat capacity of $\text{Na}_2\text{Ni}_2\text{TeO}_6$ was measured using a Quantum Designs physical properties measurement system (PPMS). Heat capacity is measured as a function of temperature using a puck based microcalorimeter where the temperature of the material is measured in response to a thermal pulse provided by a heating coil in a steady thermal environment- the semi-adiabatic relation technique (26).

The specific heat capacity (C_p) is useful in identifying the nature the magnetic transition in $\text{Na}_2\text{Ni}_2\text{TeO}_6$. There is a sharp peak present at $T = 27 \text{ K}$ in the plot of C_{diff}/T versus T that coincidences with the magnetic transition seen in magnetic susceptibility around $T_N \sim 27 \text{ K}$; this points to $\text{Na}_2\text{Ni}_2\text{TeO}_6$ having an antiferromagnetic transition at $T_N = 27 \text{ K}$. To study the magnetic contribution to the specific heat capacity of $\text{Na}_2\text{Ni}_2\text{TeO}_6$ a non-magnetic the specific heat capacity of the phonon analog $\text{Na}_2\text{Zn}_2\text{TeO}_6$ was subtracted from that of the $\text{Na}_2\text{Ni}_2\text{TeO}_6$ (C_{diff}). The specific heat plot C_p/T shows a broad curve around $T \sim 100 \text{ K}$, which is evident of the slow entropy increase that is associated with materials that have short-range magnetic ordering (27). For $\text{Na}_2\text{Ni}_2\text{TeO}_6$ the short-range order maybe due to the possible multi-phase magnetic ordering that produces magnetic domains that have high periodicity – short-range order. Magnetic entropy is plot as $S_{mag} = \int \frac{C_{diff}}{T}$ versus T where the largest rate of change is observed around the T_N temperature of 27 K . The maximum value for the magnetic entropy at the T_N is $\sim 10 \text{ J mol}^{-1}\text{K}^{-1}$ which is less than the theoretical calculated value of $S_{mag} = 18.3 \text{ J mol}^{-1}\text{K}^{-1}$. The lower entropy is indicative of the comparatively reduced number

of microstates that magnetic materials with low-dimensional (2D) magnetic ordering and short-range magnetic correlations possess (28).

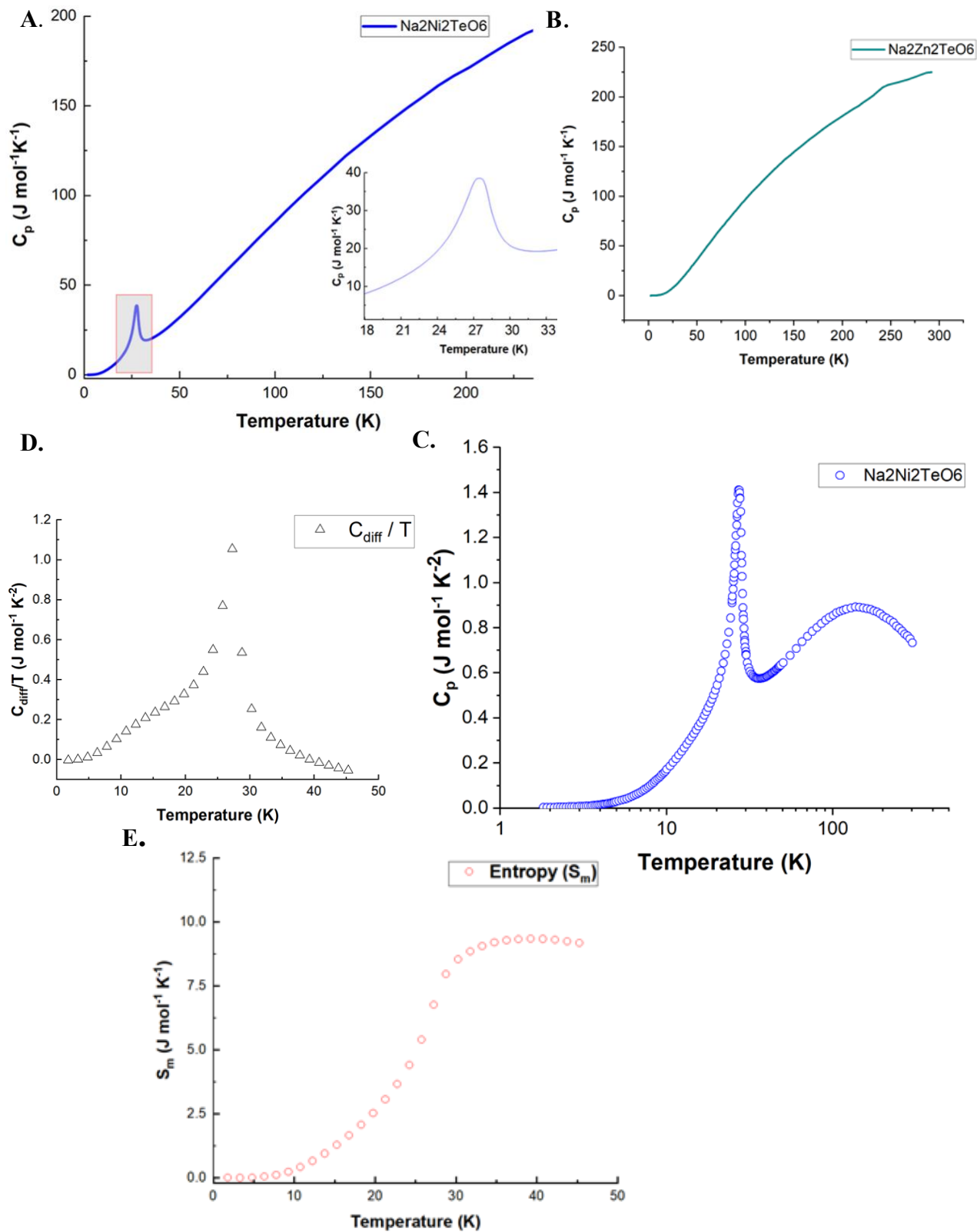


Fig (5.0) A. The C_p/T of $\text{Na}_2\text{Ni}_2\text{TeO}_6$ the inset shows a second order transition at $T = 27 \text{ K}$.
 B. C_p/T of $\text{Na}_2\text{Zn}_2\text{TeO}_6$ a phonon analog of $\text{Na}_2\text{Ni}_2\text{TeO}_6$.
 C. C_p/T of $\text{Na}_2\text{Ni}_2\text{TeO}_6$ (x-scale \log_{10}) shows a broad feature at $\sim 100 \text{ K}$ indicating short-range magnetic order transition.
 D. The C_p/T versus T of the specific heat capacity of $\text{Na}_2\text{Ni}_2\text{TeO}_6$ with specific heat capacity of $\text{Na}_2\text{Zn}_2\text{TeO}_6$ subtracted (the phonon contribution) supporting the magnetic nature of the transition at $T = 27 \text{ K}$.
 E. The magnetic entropy (S_m/T) of $\text{Na}_2\text{Ni}_2\text{TeO}_6$ with the largest change occurring around $T \approx 27 \text{ K}$.

5.2 Measuring Magnetic Susceptibility

Magnetic susceptibility is the measure of a material's magnetic polarization response to an external magnetic field. Measuring magnetic susceptibility yields a dimensionless, extensive quantity that depends on the number of magnetic moments contained in a sample's volume:

$$\chi_{vol} = \frac{M}{H} \text{ here } M \text{ is the induced magnetization the of the sample and } H \text{ is the applied magnetic}$$

field (29). To convert χ_{vol} into a more meaningful intensive quantity χ_{vol} is divided by the mass

$$\text{of the sample } g \text{ and multiplying by the samples' formal weight } F.W: \chi_{mol} = \chi_{vol} \frac{F.W}{\rho} \left(\frac{emu}{mol} \right)$$

(29). For paramagnetic, ferromagnetic, and antiferromagnetic materials magnetic susceptibility is

positive ($\chi > 0$) with ferromagnetic having the largest susceptibility and antiferromagnetic the

lowest. Diamagnetic materials produce an induced magnetic field that is opposite to the applied

field and have a negative magnetic susceptibility ($\chi < 0$) (29).

Fine magnetic susceptibility measurements are made using a vibrating sample magnetometer (VSM) with superconducting quantum interference device pick up coil (SQUID)

(29). The VSM vibrates the sample in a constant magnetic field to induce an emf in the SQUID

that is proportional to the magnetization the of the sample in accordance with Lenz's law (29).

Since the magnetization of a material is a function of thermal randomization and the strength of the applied field; magnetic susceptibility is often measured using different applied magnetic field strengths, and through a range of temperatures to fully characterize the bulk magnetic properties of a material. Zero field cooled (ZFC) measurements cool the sample below its magnetic transition temperature, a constant (DC) external magnetic field is applied, and magnetic susceptibility is measured as a function of temperature as the sample is heated. Field cooled (FC) measurements are measured as function of temperature with the sample cooled under the application of a DC field. FC magnetic susceptibility typically shows a higher magnitude over ZFC.

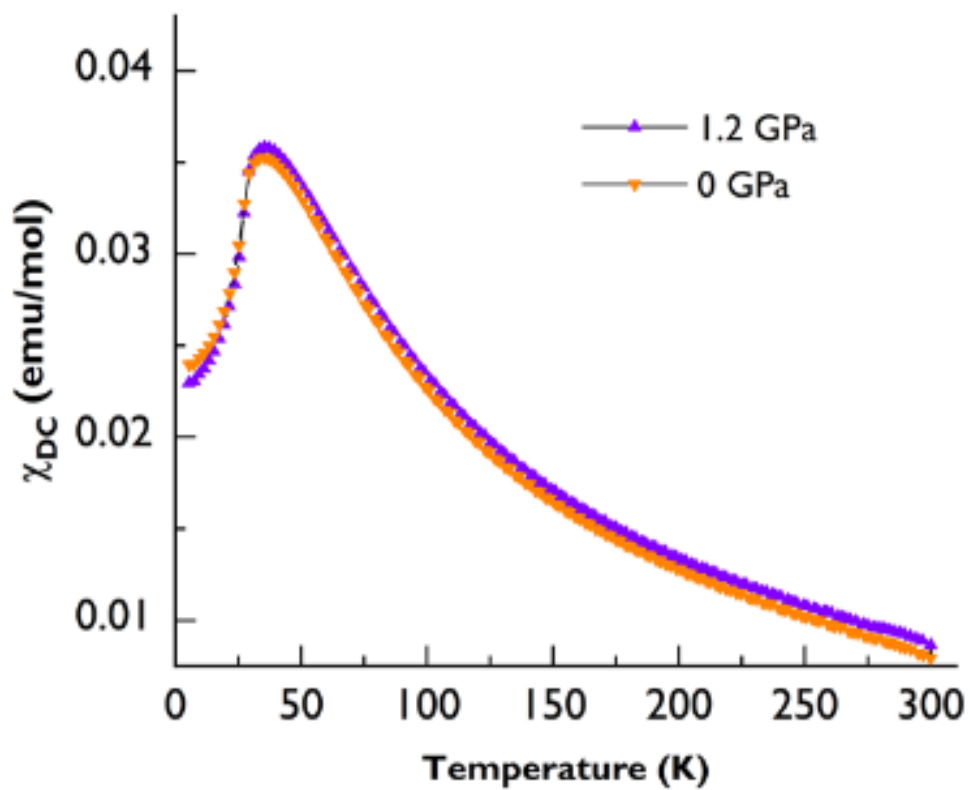
5.2.1 Curie-Weiss Law and Fitting

Curie-Weiss law is a mean field approximation for the paramagnetic phase of a materials magnetic susceptibility given by: $\chi_{mol} = \frac{C}{T - \theta}$ here C is the Curie constant T is temperature and θ is the Weiss constant (5). The Curie constant is: $C = \frac{Np^2 \mu_B^2}{3k_B}$ where N is the number of magnetic atoms p is the effective number of Bohr magnetons (μ_B) and k_B is Boltzmann's constant (5). Both the Curie and the Weiss constants can be attained from a linear extrapolation of the inverse (χ_{mol}^{-1}) susceptibility from the paramagnetic region. The Curie constant is then the inverse of the slope of the first-degree polynomial fitted to the χ_{mol}^{-1} data and the Weiss constant is the X-intercept. A ferromagnetic material has a positive Weiss constant, antiferromagnetic it is negative, and the Weiss constant is equal to zero for a paramagnetic material (5). The effective magnetic moment can be calculated using the Curie constant attained from extrapolation by the following relation $\mu_{eff} = \sqrt{8C} \mu_B / fu$, the units μ_B is the Bohr magnetons per formula unit (5).

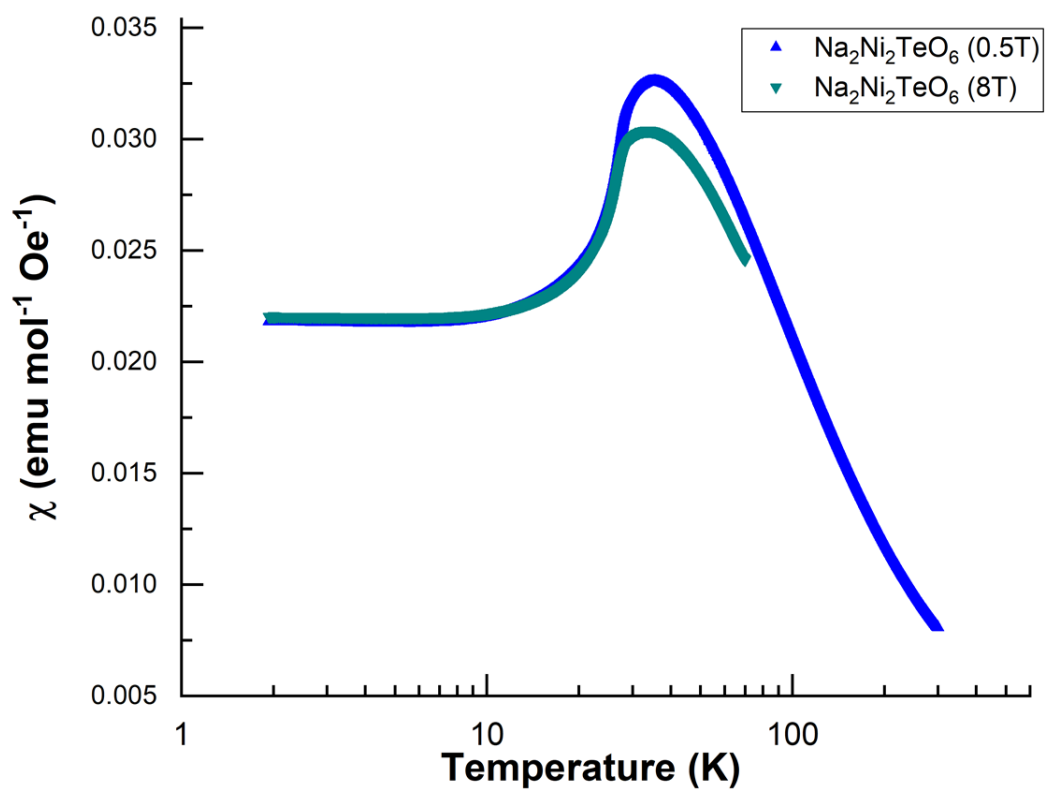
5.2.2 Magnetic Susceptibility of $\text{Na}_2\text{Ni}_2\text{TeO}_6$

The magnetic susceptibility was measured using a Quantum Designs MPMS with SQUID VSM option. Magnetic susceptibility for $\text{Na}_2\text{Ni}_2\text{TeO}_6$ measured at an applied field of 500 Oe has a broad peak that is attributed to low-dimensional magnetism that is centered around a 30 K . There is no substantial change in magnetic susceptibility at 500 Oe with application of 1.2 GPa of pressure. Additionally, measurement made at 0.5 T and 8 T do not have any major deviations from the magnetic susceptibility measurement at 500 Oe . AC magnetic susceptibility with frequency range of $0.1 - 1000 \text{ Hz}$ show no frequency dependence. Isothermal plots of magnetization versus applied field for temperatures of 5 K , 10 K , 25 K , and 60 K do not present any signature of ferromagnetism. The Curie-Weiss fit of the paramagnetic region between temperatures of 200 K and 300 K results in a Weiss constant of $\theta = -9.7(2) \text{ K}$ and effective paramagnetic moment of $\mu_{eff} = 2.2(2) \mu_B/\text{Ni}^{+2}$. The negative Weiss constant is consistent with antiferromagnetic ordering and the effective moment is close to the spin magnetic moment of Ni^{+2} $\mu_{\text{Ni}^{+2}} = 2.82 \mu_B$.

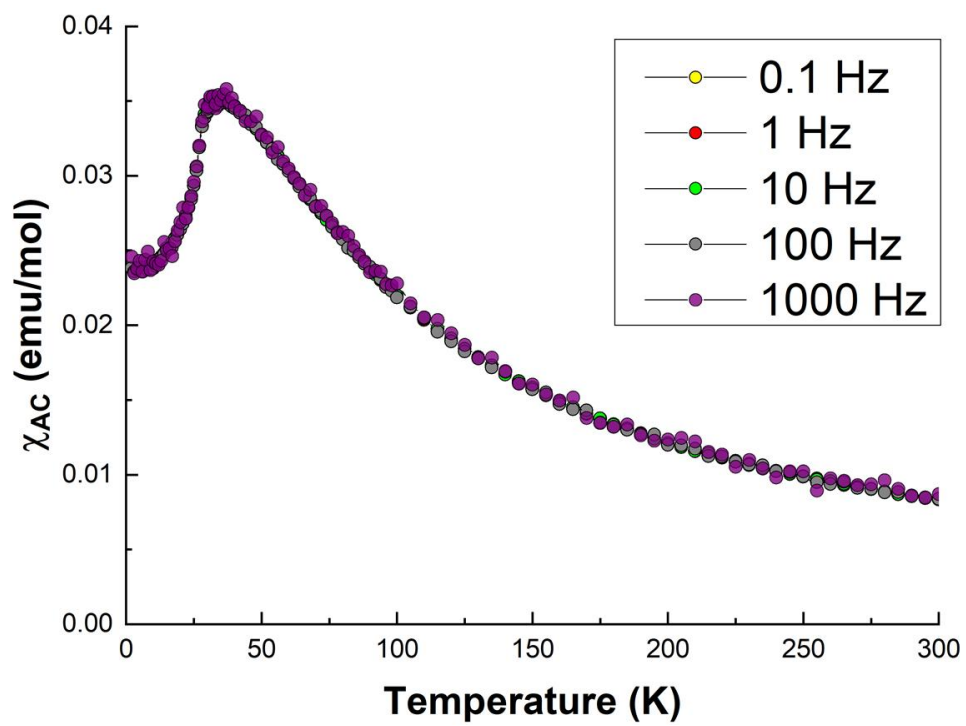
A.



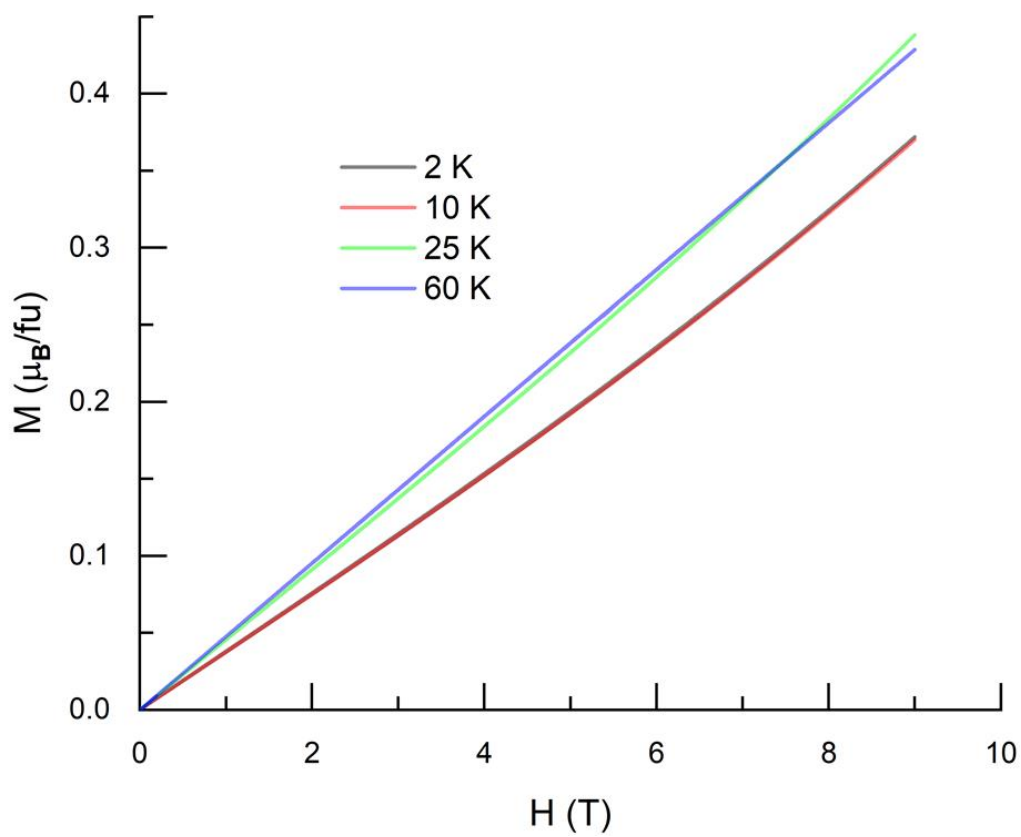
B.



C.



D.



E.

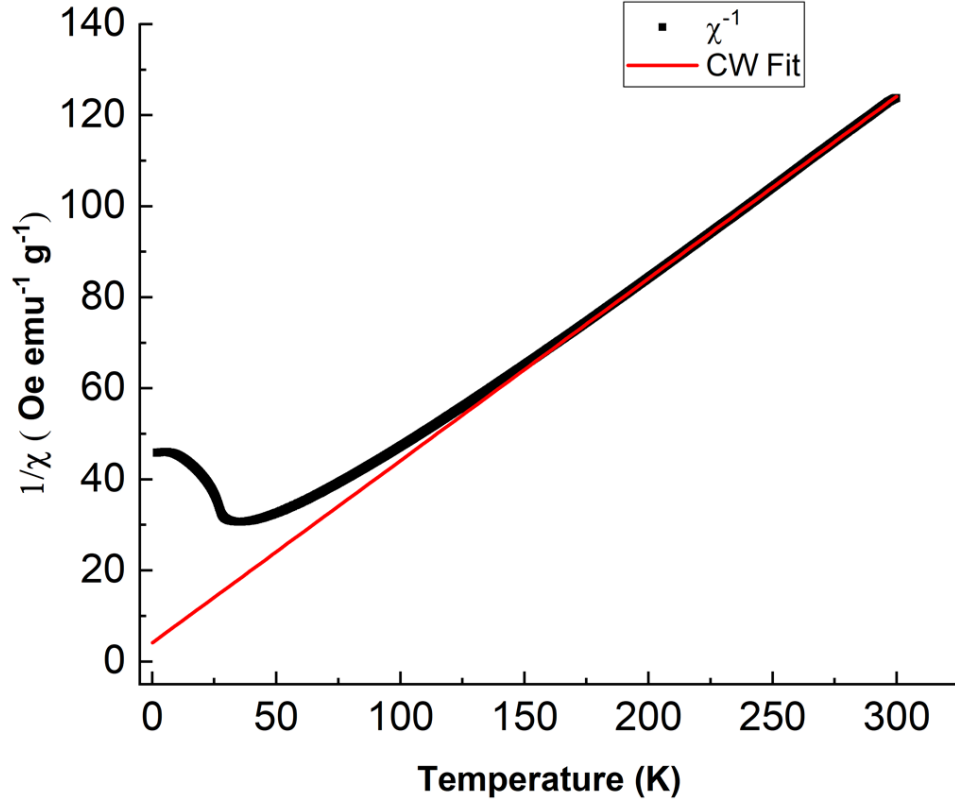


Figure. 5.2: A. Magnetic susceptibility of $\text{Na}_2\text{Ni}_2\text{TeO}_6$ at **50 Oe** with zero pressure and **1.2 Gpa**.

B. Magnetic susceptibility of $\text{Na}_2\text{Ni}_2\text{TeO}_6$ at **0.5 T** and **8 T**.

C. AC Magnetic susceptibility of $\text{Na}_2\text{Ni}_2\text{TeO}_6$ measured at **0.1 Hz**, **1 Hz**, **10 Hz**, **100 Hz**, and **1000 Hz** with an applied field of **50 Oe**.

D. Isothermal magnetization measurements at **$T = 2\text{ k}$** , **$T = 10\text{ k}$** , **$T = 25\text{ k}$** , and **$T = 60\text{ k}$** .

E. Curie-Weiss fit to inverse magnetic susceptibility.

Chapter 6: Summary and future work

The motivation for the inclusion of a short-range magnetic order component to the magnetic structure models for $\text{Na}_2\text{Ni}_2\text{TeO}_6$ comes from the observation of diffuse magnetic Bragg peaks in the low 2θ region of the $T = 5 \text{ K}$ high resolution neutron diffraction pattern. Additionally, short-range magnetic ordering is also supported by the broad feature seen in specific heat capacity around $T = 100 \text{ K}$ (27). Quantitative analysis of four magnetic structure models was carried out by Rietveld refinement of the four different magnetic phase models added to the nuclear structure. Of the four models the one that most faithfully represented the data consisted of two commensurate propagation vectors $\vec{k}_c = (0.5 \ 0 \ 0)$ and $\vec{k}_c = (0.5 \ 0 \ 0.5)$ plus short-range order. The short-range order was modeled by a Lorentzian function added to the second propagation vector. The long-range magnetic structure described by these two propagation vectors is quasi-2D with nearest neighbor Ni^{2+} magnetic moments ferromagnetically aligned on the honeycomb sublattice and antiferromagnetically aligned with next nearest neighbor Ni^{2+} moments. Thus, in ab plane, the zig-zag structure is best described by the $J_1 - J_2 - J_3$ model where J_1 and J_2 are the ferromagnet (positive) spin exchange interaction of the two nearest neighbors and the J_3 is the antiferromagnetic (negative) spin exchange interaction of the next nearest neighbor (8). We only find weak inter-layer exchange interaction in $\text{Na}_2\text{Ni}_2\text{TeO}_6$ through DFT studies (done in collaboration). The results of inelastic neutron scattering experiments on $\text{Na}_2\text{Ni}_2\text{TeO}_6$ show a spin wave excitation peak at $E = 4.52(6) \text{ meV}$ at $T = 5 \text{ K}$.

$\text{Na}_2\text{Ni}_2\text{TeO}_6$ magnetic susceptibility shows a broad antiferromagnetic magnetic transition around $T \approx 30 \text{ K}$. The Cuire-Weiss fit to the paramagnetic region of the inverse magnetic susceptibility yields a Curie-Weiss temperature of $\theta = -9.7(2) \text{ K}$ pointing to an

antiferromagnetic transition. To ascertain the magnetic transition temperature of $\text{Na}_2\text{Ni}_2\text{TeO}_6$ the magnetic degrees of freedom was isolated by subtracting the specific heat of the non-magnetic phonon analog $\text{Na}_2\text{Zn}_2\text{TeO}_6$ from $\text{Na}_2\text{Ni}_2\text{TeO}_6$ specific heat capacity. The plot of the magnetic only contribution to specific heat capacity has as sharp peak at $T_N = 27 \text{ K}$. The maximum magnetic entropy for $\text{Na}_2\text{Ni}_2\text{TeO}_6$ was calculated to be $S_{mag} \approx 10 \text{ J mol}^{-1} \text{ K}^{-1}$. The lower-than-expected value of magnetic entropy can be contributed to low-dimensional (2D) magnetic ordering and short-range magnetic correlations (28).

6.1 Future Work

Two unanswered question about the nature of the intercalated Na^+ in $\text{Na}_2\text{Ni}_2\text{TeO}_6$ from the focus for future experiments on this compound. The first question is what role, if any, does Na^{1+} have in the magnetic properties of $\text{Na}_2\text{Ni}_2\text{TeO}_6$. There exists the potential for these cations to couple with the crystal lattice or with magnetic lattice. Secondly, the diffusion mechanism of Na^+ between the metal octahedra layers in $\text{Na}_2\text{Ni}_2\text{TeO}_6$ is not studied yet. It has been suggested by Karna et al. (3) that the Na cations diffusion forms a chiral pattern as the cations transition through Na sites. A first-principles computational study of two similar compounds $\text{Na}_2\text{Mg}_2\text{TeO}_6$ and $\text{Na}_2\text{Zn}_2\text{TeO}_6$ found that the diffusion occurs in a linear fashion with the aid of phonon modes (31). To clarify the Na^{1+} diffusion mechanism back scattering neutron experiments need to be conducted.

References

- 1) Evstigneeva, Maria A., et al. "A new family of fast sodium ion conductors: Na₂M₂TeO₆ (M= Ni, Co, Zn, Mg)." *Chemistry of Materials* 23.5 (2011): 1174-1181.
- 2) Kurbakov, Alexander I., et al. "Long-range and short-range ordering in 2D honeycomb-lattice magnet Na₂Ni₂TeO₆." *Journal of Alloys and Compounds* 820 (2020): 153354.
- 3) Karna, Sunil K., et al. "Sodium layer chiral distribution and spin structure of Na₂Ni₂TeO₆ with a Ni honeycomb lattice." *Physical Review B* 95.10 (2017): 104408.
- 4) Sankar, R., Muthuselvam, I. P., Shu, G. J., Chen, W. T., Karna, S. K., Jayavel, R., & Chou, F. C. (2014). Crystal growth and magnetic ordering of Na₂Ni₂TeO₆ with honeycomb layers and Na₂Cu₂TeO₆ with Cu spin dimers. *CrystEngComm*, 16(47), 10791-10796
- 5) Kittel, C. Introduction to solid state physics/Charles Kittel. 5th
- 6) Takagi, H., Takayama, T., Jackeli, G., Khaliullin, G., & Nagler, S. E. (2019). Concept and realization of Kitaev quantum spin liquids. *Nature Reviews Physics*, 1(4), 264-280.
- 7) Kitaev, A. (2006). Anyons in an exactly solved model and beyond. *Annals of Physics*, 321(1), 2-111.
- 8) Fouet, J. B., Sindzingre, P., & Lhuillier, C. (2001). An investigation of the quantum J₁-J₂-J₃ model on the honeycomb lattice. *The European Physical Journal B-Condensed Matter and Complex Systems*, 20(2), 241-254.
- 9) Lee, K. H., Chung, S. B., Park, K., & Park, J. G. (2018). Magnonic quantum spin Hall state in the zigzag and stripe phases of the antiferromagnetic honeycomb lattice. *Physical Review B*, 97(18), 180401.
- 10) Hannay, N. B. (1973). Treatise on solid state chemistry. Plenum Press.
- 11) West, A. R. (2014). Solid state chemistry and its applications. John Wiley & Sons
- 12) Méndez, C., Podestá, J. M., Toro, S., Huespe, A. E., & Oliver, J. (2019). Making use of symmetries in the three-dimensional elastic inverse homogenization problem. *International Journal for Multiscale Computational Engineering*, 17(3).
- 13) Sweet, R. (2020, September 01). *Fundamentals of Crystallography*. Lecture presented at BNL On-line Graduate Course 2020 in Brookhaven National Laboratory, Upton.

- 14) Designua. (2016, February 02). Waves Diffraction stock vector. Illustration of direction - 65914893. Retrieved January 17, 2021, from <https://www.dreamstime.com/stock-illustration-waves-diffraction-interference-occurs-wave-passes-edge-passes-narrow-gap-goes-past-image65914893>
- 15) Harvey, J., & Pfisterer, R. (n.d.). Understanding diffraction grating behavior: Including conical diffraction and Rayleigh anomalies from transmission gratings. Retrieved January 17, 2021, from <https://www.spiedigitallibrary.org/journals/optical-engineering/volume-58/issue-08/087105/Understanding-diffraction-grating-behavior--including-conical-diffraction-and-Rayleigh/10.1117/1.OE.58.8.087105.full?SSO=1>
- 16) Speakman, S. A., Ph.D. (2021, February 17). *Basics of X-Ray Powder Diffraction*. Lecture presented at Training to Become an Independent User of the X-Ray SEF at the Center for Materials Science and Engineering at MIT in MIT, Boston.
- 17) T. (2016, December 30). Bragg law. Retrieved January 17, 2021, from <https://www.britannica.com/science/Bragg-law>
- 18) Heitmann, T., & Montfrooij, W. (2012). *Practical Neutron Scattering at a Steady State Source*. Columbia, Missouri: Mizzou Media.
- 19) P. (2017, August 15). *Characteristic X-rays of copper* [PDF]. Göttingen, Deutschland: PHYWE Systeme GmbH & Co.
- 20) BM Description. (2018, May 09). Retrieved January 28, 2021, from <https://11bm.xray.aps.anl.gov/description.html>
- 21) Lutterotti, L. (2021, February 17). *Introduction to diffraction and the Rietveld method*. Lecture presented in Corso: Laboratorio Scienza e Tecnologia dei Materiali, Via Verdi 8 10124 Torino.
- 22) Wills, A. (2017, December 05). Software. Retrieved April 05, 2021, from <http://fermat.chem.ucl.ac.uk/spaces/willsgroup/software/>
- 23) Korshunov, A., Safiulina, I., & Kurbakov, A. (2020). Spin Correlations and Short-Range Magnetic Order in the Honeycomb-Layered Na₂Ni₂TeO₆. *physica status solidi (b)*, 257(3), 1900232.
- 24) Kurbakov, A. I., Korshunov, A. N., Podchezertsev, S. Y., Stratan, M. I., Raganyan, G. V., & Zvereva, E. A. (2020). Long-range and short-range ordering in 2D honeycomb-lattice magnet Na₂Ni₂TeO₆. *Journal of Alloys and Compounds*, 820, 153354.

- 25) Cengel, Y. A., & Boles, M. A. (2007). *Thermodynamics: An Engineering Approach* 6th Edition (SI Units). The McGraw-Hill Companies, Inc., New York.
- 26) Design, Q. (2019). Physical property measurement system. Retrieved April 19, 2021, from <https://www.qdusa.com/products/ppms.html>
- 27) Sharma, S., Basu, T., Shahee, A., Singh, K., Lalla, N. P., & Sampathkumaran, E. V. (2014). Multiglass properties and magnetoelectric coupling in the uniaxial anisotropic spin-cluster-glass $\text{Fe}_{2}\text{TiO}_{5}$. *Physical Review B*, 90(14), 144426.
- 28) Carlin, R. L. (2012). *Magnetochemistry*. Springer Science & Business Media.\
- 29) Coey, J. M. (2010). *Magnetism and magnetic materials*. Cambridge university press.
- 30) Brown, C. (2019, March 5). High resolution powder diffractometer - bt-1. Retrieved April 27, 2021, from <https://www.nist.gov/ncnr/high-resolution-powder-diffractometer-bt-1>

Vita

I earned my Bachelor of Science degree from NMSU in Engineering Physics in December 2017. My concentration was in mechanical engineering and I minored in nuclear chemical engineering.

At UTEP (Jan 2019 – Present) I have been a teaching assistant for the department of physics, and the mechanical engineering department. My duties have included: proctoring exams, tutoring, and grading. I have also been a research assistant (May – Aug 2019, May – Aug 2020) in the Strongly Correlated Materials Lab, UTEP Department of Physics where gained experience in the following: Powder X-Ray Diffraction and Data Analysis, Solid-State Materials Synthesis, Crystal Growth (Flux-Melt and Optical Float-Zone), Lab Equipment and Supplies Procurement, Hazardous Materials Handling

While at UTEP I have earned to academic awards; the C. Sharp Cook Graduate Physics Scholarship (2019) and the Dodson graduate Research Grant (2020). I have gone on two research trips to conduct neutron scattering experiments once to MURR (Inelastic neutron scattering), and to POWGEG SNS ORNL (neutron diffraction).

I have given two poster presentations: *Phase transitions in novel Li-containing honeycombs, $\text{Li}_8\text{Cr}_2(\text{Sb/Te})_2\text{O}_{12}$* 10th American Conference on Neutron Scattering (ACNS 2020), and *Magnetism in the Honeycomb Layers of $\text{Na}_2\text{Ni}_2\text{TeO}_6$ with Chiral Layers of Na* 2020 VIRTUL MRS SPRING/FALL MEETING & EXHIBIT

While working on my master's at UTEP I have two publications for my work thus far:

Long- and short-range ordered magnetism in honeycomb $\text{Na}_2\text{Ni}_2\text{TeO}_6$: Insights from density functional theory and neutron scattering Nathan Episcopo, et al. (Journal of Physics: Condensed Matter)

Absence of long-range magnetic order in lithium-containing honeycombs in the Li-Cr-(Te/Sb)-O system Mandujano, Hector; Gonzalez, et al. (Journal of Physics: Condensed Matter)

Nathan Episcopo

nepeiscopo@miners.utep.edu